Influence of different type of impermeable phase on the permeability of PLA films: Nanofillers versus crystalline phase

Aurore Jullin, Guillaume Sudre, Nicolas Hascoët, Francisco Chinesta, Eliane Espuche

▶ **To cite this version:**

Aurore Jullin, Guillaume Sudre, Nicolas Hascoët, Francisco Chinesta, Eliane Espuche. Influence of different type of impermeable phase on the permeability of PLA films: Nanofillers versus crystalline phase. Polymer Testing, 2025, 142, pp.108682. ⟨10.1016/j.polymertesting.2024.108682⟩. ⟨hal-04922686⟩

HAL Id: hal-04922686

https://hal.science/hal-04922686v1

Submitted on 9 Apr 2026

HAL is a multi-disciplinary open access archive for the deposit and dissemination of scientific research documents, whether they are published or not. The documents may come from teaching and research institutions in France or abroad, or from public or private research centers.

L'archive ouverte pluridisciplinaire **HAL**, est destinée au dépôt et à la diffusion de documents scientifiques de niveau recherche, publiés ou non, émanant des établissements d'enseignement et de recherche français ou étrangers, des laboratoires publics ou privés.

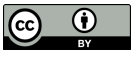

Distributed under a Creative Commons CC BY 4.0 - Attribution - International License

Polymer Testing 142 (2025) 108682

Contents lists available at ScienceDirect

Polymer Testing

journal homepage: www.elsevier.com/locate/polytest

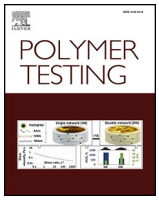

Influence of different type of impermeable phase on the permeability of PLA films: Nanofillers versus crystalline phase

Aurore Jullin [a], Guillaume Sudre [a], Nicolas Hascoët [b], Francisco Chinesta [b], Eliane Espuche [a,*]

[a] Universite Claude Bernard Lyon 1, INSA Lyon, Université Jean Monnet, CNRS, UMR 5223, Ingénierie des Matériaux Polymères, F-69622 Villeurbanne Cedex, France
[b] Arts et Métiers Institute of Technology, PIMM, 151 Boulevard de L'hôpital, F-75013, France

ARTICLE INFO

Keywords:
Nanocomposites
Polylactic acid
Crystalline phase
Water vapor permeability
Modeling

ABSTRACT

Different amorphous PLA-based nanocomposites series allowing to vary the nanofiller shape from spherical (hydrophobic/hydrophilic silica, silver), to tubular (halloysites) and lamellar (montmorillonite, graphene) have been prepared for filler content up to 15 vol%. In parallel, a semi-crystalline PLA films series has been prepared by annealing amorphous PLA films from the glassy state with the aim to achieve different degree of crystallinity. The polymer chains mobility and the impermeable domains (either filler domains or crystalline phase) contained in each membrane have been characterized in detail. Membranes water vapor and oxygen permeability coefficients have been determined with the aim to evidence the governing factors for barrier properties. For nanocomposite membranes, the matrix microstructure and chain mobility were not significantly affected by the addition of fillers, so the barrier properties were mainly governed by the filler domains size and dispersion. For semi-crystalline membranes, the increase in crystallinity led to a decrease of the amorphous chains mobility (*MAF*) which was found to also influence the permeability. Theoretical models were used to describe the evolution of the experimental relative permeability and an equivalence diagram was proposed to have a direct comparison of the effect of fillers and crystallinity on the permeability.

1. Introduction

Polymers are attractive materials because of their low cost, ease of processing and low density. However, the significant environmental footprint of petroleum-based polymers, and particularly the large amount of waste produced by packaging, has led to a growing interest in biodegradable polymers. Poly(lactic acid) (PLA) combines the advantages of being both bio-sourced and biodegradable and is therefore a promising alternative to replace petroleum-based polymers for short-term applications such as packaging. Although PLA accounts for 60 % of the total quantity of biodegradable polymers produced for packaging in 2023 [1], one of the obstacles to greater market penetration is its low gas and water barrier properties [2–4]. Faced with this challenge, lot of studies focused on barrier improvement by adding an impermeable dispersed phase within the permeable continuous polymer phase with the aim to lengthen the diffusion path and decrease the permeable phase content.

In this context, PLA nanocomposites containing impermeable nanofillers have been developed in the last decades. If the efficiency of lamellar type nanofillers as a mean to bring a significant tortuosity effect has been shown by several authors [5–9] it has to be noticed that only few works focused on the use of spherical or nanotube-type fillers [10–13]. The performances of the nanocomposite materials are usually discussed as a function of the introduced fillers (aspect ratio, volume fraction, dispersion state), the polymer chain mobility and the filler/-matrix interface [10,14–18]. It is noteworthy that the comparison between barrier properties obtained from different fillers is rarely performed and it is often limited to two or three filler types, such as montmorillonite versus nanocellulose nanocrystals and nanofibers [19,20] or montmorillonite versus halloysite nanotubes [21].

Another way of inducing the presence of an impermeable phase within a polymer matrix is to anneal the polymer in order to create a crystalline phase. Due to its significantly higher density than the amorphous phase, the crystalline phase is usually considered as an impermeable phase [10,22–25]. Moreover, modification of the chain mobility at the crystalline/amorphous region can also occur and be

* Corresponding author.
E-mail address: eliane.espuche@univ-lyon1.fr (E. Espuche).

https://doi.org/10.1016/j.polymertesting.2024.108682
Received 21 October 2024; Received in revised form 5 December 2024; Accepted 26 December 2024
Available online 26 December 2024
0142-9418/© 2025 The Authors. Published by Elsevier Ltd. This is an open access article under the CC BY license (http://creativecommons.org/licenses/by/4.0/).

estimated through the mobile amorphous fraction (*MAF*) with respect to the rigid amorphous fraction (*RAF*) [26,27]. Although some studies focused on the effect of the crystalline phase on PLA permeability [24–27], showing a global increase of barrier properties with the increase of the crystallinity, no detailed relations were established neither with the crystalline morphology nor with the *MAF/RAF* contents.

The aim of the present work is to prepare and finely characterize a PLA-based material platform in which each material series contains a specific type of dispersed impermeable phase. For that goal, different amorphous PLA-based nanocomposite series containing either lamellar (montmorillonite, graphene), spherical (hydrophobic/hydrophilic silica, silver) or halloysite nanotubes were prepared by melt-blending for filler content up to 15 vol%. Semi-crystalline PLA samples with increasing degree of crystallinity have also been prepared by annealing reference amorphous PLA films. Morphology as well as PLA chain mobility are deeply investigated for each materials series. Oxygen and water vapor permeability coefficients of the different samples are determined and discussed as a function of the material structural parameters. From this experimental analysis, the governing factors of the transport are identified for each materials series and allow to choose for each PLA-based materials series, the appropriate physical models enabling to predict accurately the permeability data. Finally, a permeability diagram allowing to easily establish equivalence laws between the different investigated impermeable phases is proposed. According to our knowledge, it is the first time that such a large material platform is prepared and investigated, going from experimental to modeling approach, with the aim to compare the effects of different types of impermeable phases on PLA barrier properties.

2. Experimental

2.1. Materials

Poly(lactic acid) PLA 2003D, containing 4.1 mol% of D-isomers and with a density of 1.25, was provided by NatureWorks LLC. The number average molar mass, M_n, was determined by size exclusion chromatography and is equal to 86 000 g/mol. Different impermeable nanofillers were selected in order to cover a wide range of filler shapes going from spheres to tubes and platelets (Fig. 1). Their main characteristics are summarized in Table 1.

2.2. PLA neat films and nanocomposites preparation

PLA nanocomposites were prepared by melt-blending using a Haake internal mixer. Compounding was carried out at a set-point temperature of 185 °C and a rotation speed of 50 rpm. The residence time was fixed at 10 min. The nanofillers content ranged from 0 to 15 vol%. Unfilled PLA was melt-processed in the same conditions to prepare a reference material. Then 130 ± 10 μm films were prepared from each compound by compression molding at 180 °C under 150 bars for 2 min, with 4 min of preheating. To obtain amorphous films, samples were placed between two metal plates at room temperature after thermo-compression and cooled under compressed air for few minutes. As PLA is very sensitive to hydrolysis during melt processing, all materials (PLA granular, nanofillers as well as the compounds) were dried at least 24 h in a vacuum oven at 85 °C before each processing step (melt compounding and compression molding).

Semi-crystalline PLA films with different degrees of crystallinity were prepared from PLA amorphous films by annealing in an oven at T_a = 110 °C or 120 °C for durations varying between 0 and 24 h.

In this work, reference amorphous PLA film is denoted PLAref, nanocomposites films are referred as PLA/filler type/X where X is the volume content of the filler and semi-crystalline PLA films are named PLA/T_a/χ_c where T_a is the annealing temperature and χ_c is the degree of crystallinity. Table 2 summarizes the different films series investigated in this work.

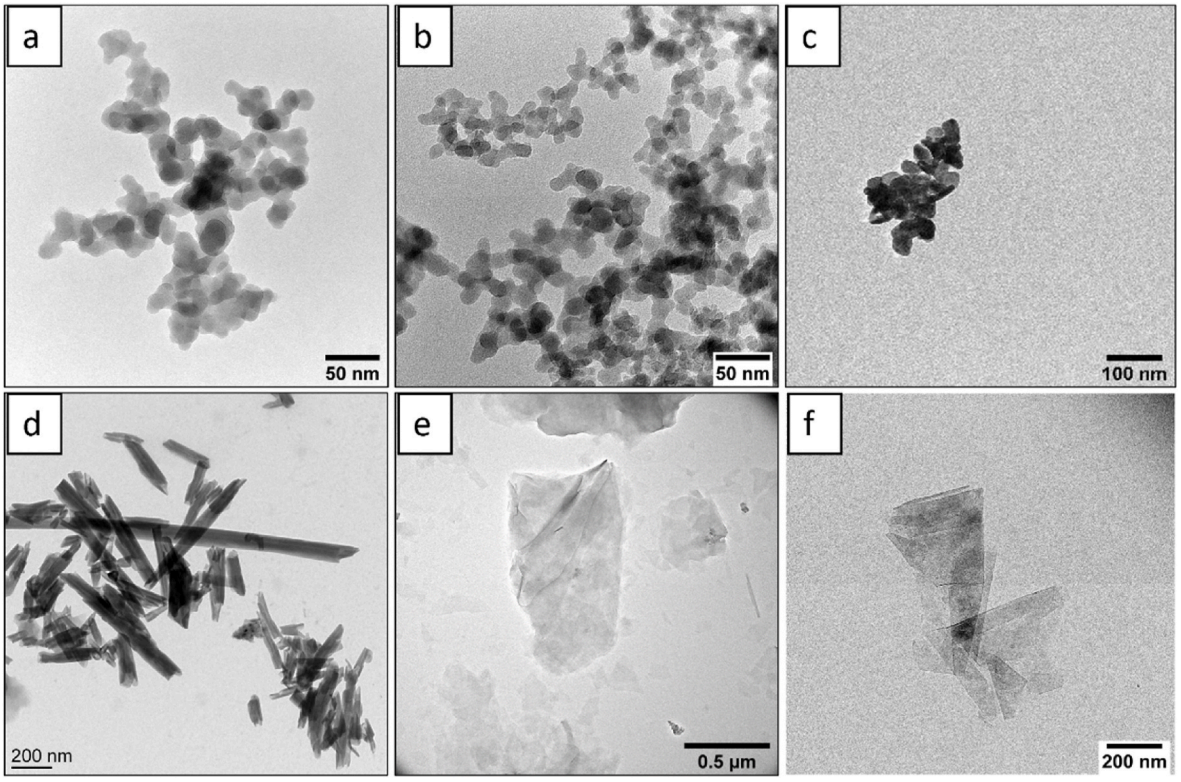

Fig. 1. TEM micrographs of the selected fillers: a) hydrophilic silica, b) hydrophobic silica; c) silver, d) halloysite nanotubes, e) organo-modified montmorillonite and f) graphene.

Table 1
Characteristics of the selected fillers (d stands for the mean diameter, L: the mean length, w: the mean thickness of the elementary fillers).

Nanofiller type	Nomenclature	Commercial name/supplier	Dimensions/shape	Surface modification	Density
Hydrophilic silica	SiOH	Aerosil® 200/Evonick Operations GmbH	$d = 20 \pm 5$ nm **Sphere**	/	2.2 [28]
Hydrophobic silica	$SiCH_3$	Aerosil® AR974/Evonick Operations GmbH	$d = 20 \pm 5$ nm **Sphere**	Dimethyl dichlorosilane (0.7–1.3 wt% carbon)	2.2 [28]
Organo modified montmorillonite	OMMT	Cloisite® 30B /Southern Clay Product	$L = 200$ nm $w = 1$–2 nm **Platelet**	Methyl tallow bis-2-hydroxyethyl, quaternary ammonium (29 wt%) CEC = 90 meq/100 g	1.98 [7]
Halloysite nanotubes	HNT	Halloysite nanotubes/Sigma-Aldrich	$L = 300$–1000 nm d ≈ 40 nm **Tubes**	/	2.53 [29]
Silver nanoparticles	Ag	Silver Metal Nanopowder (99.9 % metal basis)/American Element	$d = 35 \pm 5$ nm **Sphere**	/	10.5 [30]
Graphene oxide	GNP	KNG-180-3 Graphene oxide Nanoplatelets Knano (Xianen, China)	L = 500–1000 nm $w \approx$ 1 nm **Platelet**	/	2.2 [31]

Table 2
Name of the different PLA -based films.

Sample name	Type of impermeable phase	Range of impermeable phase content (vol%)
PLAref	/	0
PLA/SiOH/X	Hydrophilic silica	0–4
PLA/$SiCH_3$/X	Hydrophobic silica	0–10
PLA/Ag/X	Silver metal powder	0–4
PLA/OMMT/X	Organo modified montmorillonite	0–15
PLA/HNT/X	Halloysite nanotubes	0–10
PLA/GNP/X	Graphene platelets	0–1.5
PLA/T_a/χ_c	PLA crystalline phase	0–50

2.3. Characterization methods

2.3.1. Size exclusion chromatography (SEC)

PLA average molar masses were measured for the different samples by SEC analyses. First, samples were dissolved in chloroform (3 mg/mL) and the solutions were filtered on a PTFE filter plate (pore size = 0.45 μm) before analysis. Then, SEC analyses were carried out with a Polymer Lab type C mixed PLgel column (length = 30 cm, diameter = 7.8 mm, stationary phase 5 PSDVB, temperature = 25 °C, feed rate = 0.5 mL/min, separation performance = 2.10^2–2.10^6 g/mol). The refraction index and the light diffusion were measured respectively by Shimadzu RID20 and TREOS Wyatt sensor.

2.3.2. Thermal analysis

Thermogravimetric analyses (TGA) were performed by using a Mettler Toledo TGA/DSC 1 STAR^e System to determine the degradation temperature of the nanocomposites and the nanofillers content. The samples were heated from 25 to 500 °C at 10 °C/min under dry nitrogen flow. The weight loss was recorded as a function of the temperature. The onset degradation temperature was determined by using the tangent method. The nanofiller volume content (ϕ_v) was determined from the mass residues at the 500 °C plateau, the density of the PLA and the density of the filler. For nanocomposites filled with Cloisite® 30B, the mass content of the organic cation (30 wt%) was added to the residual mass for volume fraction calculations.

Differential scanning calorimetry (DSC) experiments were performed by using a TA Instrument Q200 calorimeter calibrated with indium standard. Experiments were conducted under nitrogen flow (50 mL/min). Samples (5–10 mg) were placed in an aluminum pan. The melting behavior was investigated through experiments performed with a heating ramp from 25 to 200 °C at 10 °C/min using a standard mode. The degree of crystallinity (χ_c) of the PLA was calculated according to Equation (1):

$$\chi_c = \frac{\Delta H_m - \Delta H_{cc}}{\Delta H_{m\infty}(1-\phi_m)} \quad (1)$$

where ΔH_m is the enthalpy of melting, ΔH_{cc} is the enthalpy of cold crystallization, Φ_m the mass fraction of fillers and $\Delta H_{m\infty}$ is the enthalpy of the infinite crystal with a value of 93 J/g [32]. The analysis of the PLA glass transition was performed by Temperature Modulated Differential Scanning Calorimetry, using a modulated temperature program. The samples were heated from 10 to 90 °C at an average heating rate of 2 °C/min with an oscillation amplitude of 0.318 °C (heat mode only) and a period of 60 s [26]. The glass transition temperature was taken at the onset of the transition. The ΔC_p value was calculated from the onset to the end of the glass transition. The quantity of mobile amorphous fraction (*MAF*) was determined according to Equation (2):

$$MAF = \frac{\Delta C_p}{\Delta C_{p0}\,(1-\phi_m)} \quad (2)$$

Where Φ_m is the mass fraction of fillers, ΔC_p the heat capacity change of the studied sample and ΔC_{p0} the heat capacity change of the amorphous PLA. The quantity of rigid amorphous fraction (RAF) was calculated according to Equation (3).

$$RAF = 1 - MAF - \chi_c \quad (3)$$

The uncertainties on the degree of crystallinity as well as on the *MAF* and the *RAF* have been calculated by uncertainties propagation of the heat capacity and the enthalpy.

2.3.3. PLA microstructure analysis

The crystalline structure of annealed PLA was investigated by small and wide-angle X-ray scattering (SAXS/WAXS). Experiments were performed at the European Synchrotron Radiation Facility (ESRF, Grenoble, France) on the BM02 beamline. The incident photon energy was 15.7 keV ($\lambda = 0.77$ Å). The sample-to-detector distance was respectively about 23 cm for the WAXS and 3.15 m for the SAXS, and the chosen beam stop had a diameter of 2.5 mm. The q-range of SAXS was calibrated using silver behenate and that of WAXS using LaB_6. The contribution of the empty cell was subtracted from the scattering images of the studied samples, and the intensity was normalized by sample thickness and azimuthally averaged to obtain I *vs.* q, where I is the signal intensity and q is the diffusion vector.

The morphology of the semi-crystalline PLA has also been characterized by scanning electron microscopy (SEM) observations with a voltage of 5 kV using a Secondary Electron detector. Before observations, the samples surfaces were prepared with a Leica Ultracut B microtome at room temperature using oscillating diamond knife. The samples were then etched with chloroform vapor for 28 min to partially

dissolve the amorphous phase.

2.3.4. Nanofiller dispersion analysis

Nanofiller dispersion in the films cross section was observed by Transmission Electron Microscopy (TEM). The nanocomposite films were ultramicrotomed with oscillating diamond knife (Diatom, 35°) on a Leica Ultracut B microtome at room temperature with a knife speed between 0.8 and 1.2 mm/s to give section thickness of 60–70 nm. The sections were then transferred on a 200-mesh copper grid with a carbon membrane. The TEM bright field observations were performed on a JEOL-1400 flash microscope operating at 120 kV. For nanocomposites based on halloysite nanotubes, the filler dispersion was observed in the cross section and parallel to the film surface.

For nanocomposites films containing spherical or halloysite fillers, ImageJ software as well as Scikit-image processing in Python were used to measure the diameters, the area, the aspect ratio, and the number of impermeable domains per surface unity in the different samples. In the case of Cloisite® 30B and graphene, due to lack of contrast and the complexity of the filler domain shapes, the proportion as well as the aspect ratio of different classes of filler domains were measured manually with ImageJ software. The interparticle distance for all the nanocomposites was also measured manually using ImageJ software. For all samples, the mean values of each morphological parameter were determined from the analysis of at least 60 filler domains.

2.3.5. Permeability measurements

Permeability measurements were performed on samples of 5 cm^2 effective area. Oxygen transmission rate (OTR in $cm^3{}_{STP}$.cm/[cm^2-day]) was measured at 23 °C and 0 % relative humidity with a MOCON OXTRAN®. The test cell was composed of two chambers separated by the film. Nitrogen containing 2 % of hydrogen (N_2/H_2) was used as the carrier gas and pure oxygen was used as the test gas. Before each measurement, a nitrogen purge (flow of 10 mL/min) during 48 h was realized to remove trace of atmospheric oxygen. Oxygen was then introduced at 20 mL/min and the oxygen flux going through the film was measured by a coulometric sensor.

Water vapor transmission (WVTR in g/[m^2. day]) was measured at 23 °C and 90 % relative humidity with a MOCON PERMATRAN W3/33 equipped with an infrared sensor. Water transfer though the films was conducted by N_2 gas at 100 sccm to the infrared sensor.

In all cases, the permeability P is calculated from the steady state flux J according to Equation (4):

$$P = \frac{J.e}{\Delta p} \tag{4}$$

where e is the sample thickness (cm), taken from the average value of five measurements and Δp the difference of pressure between the upstream and the downstream compartments (cmHg). The permeability coefficient P is expressed in Barrer units (1 Barrer = 10^{-10} cm^3_{STP}.cm. $cm^{-2}.s^{-1}.cmHg^{-1} = 3.36.10^{-16}$ mol m $m^{-2}.s^{-1}.Pa^{-1}$).

3. Results and discussion

3.1. Morphological characterization of the reference and nanocomposite films series

3.1.1. Reference amorphous PLA films

PLA films prepared according to the same processing conditions as the nanocomposite films are used as reference and were characterized.

The number average molar mass of PLA after the melt blending and compression step was similar to that one of the PLA granular (86 000 g/mol) showing that no significant degradation occurred during the processing step. The TGA thermogram of the reference PLA film is given in Fig. 2. The degradation begins at 348 °C and the subsequent mass loss observed corresponds to hydrolysis of the PLA chains and then a decomposition of the oligomers [33]. The residue at 500 °C is equal to 0 %.

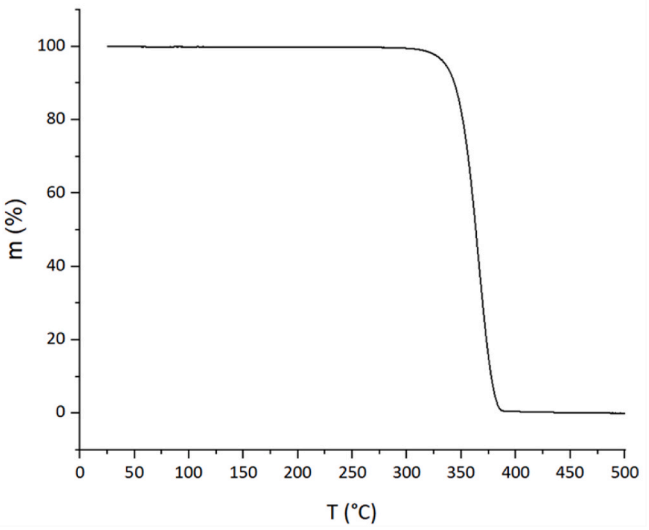

Fig. 2. TGA thermogram of the reference PLA film at 10 °C/min under nitrogen.

The DSC thermogram (Fig. 3) shows the glass transition temperature (T_g) of the reference film at 56 ± 1 °C which is in agreement with values reported in the literature [6,10]. The small endothermic peak observed at the glass transition, is assigned to physical aging phenomenon [34]. The thermogram exhibits at higher temperature an exotherm associated with the PLA cold crystallization (T_{cc} = 118 ± 2 °C) and a melting peak (T_m = 150 ± 2 °C). The values of the different transitions reported in the present work are similar to those found in the literature for PDLLA processed and characterized under similar conditions [6,10,24]. Moreover, the amorphous nature of the reference film is confirmed as the melting enthalpy and the cold crystallization enthalpy have the same value ($\Delta H_{cc} = \Delta H_f$ = 24 ± 2 J/g). The ΔC_{p0} value of the reference amorphous PLA was fond to be 0.52 ± 0.02 J $g^{-1}°C^{-1}$ in agreement with the study of Guinault et al. on PDLLA [24].

3.1.2. Nanocomposite films

Table 3 summarizes the values of the average molar mass of the reference PLA and of the most highly filled material for each studied nanocomposites series as well as the data (degradation temperature and mass residue at 500 °C) obtained from TGA.

The M_n values measured for PLA/$SiCH_3$/10, PLA/Ag/4, PLA/HNT/

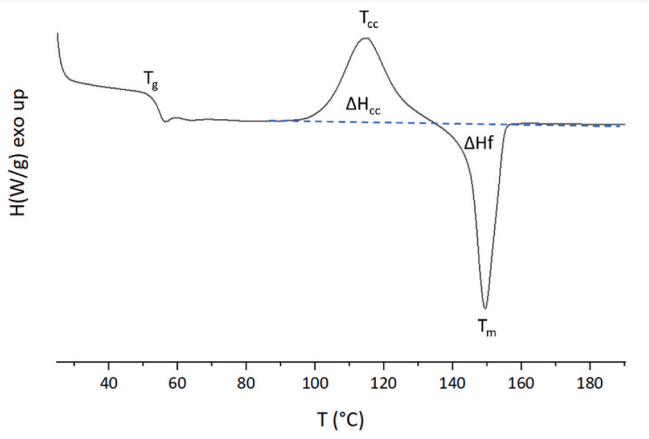

Fig. 3. DSC thermogram of the reference PLA film corresponding to the first heating performed at 10 °C/min.

Table 3
Matrix number average molar mass, degradation temperature at the onset and mass residue determined for the different nanocomposite series.

Sample	Mn (10^3 g/mol)	$T_{d\ onset}$ (°C)	Mass residue at 500 °C (%)
PLAref	87 ± 3	348 ± 1	0
PLA/SiOH/1	/	347 ± 1	1.2
PLA/SiOH/3	/	347 ± 1	5.2
PLA/SiOH/4	/	347 ± 1	6.5
PLA/$SiCH_3$/1	/	347 ± 1	1.5
PLA/$SiCH_3$/4	/	347 ± 1	7.0
PLA/$SiCH_3$/5	/	347 ± 1	8.0
PLA/$SiCH_3$/10	77 ± 6	347 ± 1	16.3
PLA/Ag/0.5	/	348 ± 1	3.9
PLA/Ag/1	/	346 ± 1	5.2
PLA/Ag/3	/	342 ± 1	20.8
PLA/Ag/4	79 ± 5	340 ± 1	26.3
PLA/HNT/0.5	/	348 ± 1	1.2
PLA/HNT/2	/	343 ± 1	3.8
PLA/HNT/4	/	342 ± 1	7.5
PLA/HNT/10	71 ± 5	337 ± 1	18.3
PLA/OMMT/2.5	50 ± 3	347 ± 1	3.0
PLA/OMMT/5	/	345 ± 1	6.3
PLA/OMMT/10	/	343 ± 1	10.9
PLA/OMMT/15	58 ± 7	341 ± 1	14.9
PLA/GNP/0.05	/	347 ± 1	<0.1
PLA/GNP/0.1	/	347 ± 1	0.14
PLA/GNP/0.5	/	346 ± 1	0.87
PLA/GNP/1.5	85 ± 3	348 ± 1	2.7

10 and PLA/GNP/1.5 are in the same range, close to the value obtained for the reference PLA film. PLA films filled with OMMT exhibit a lower M_n indicating a higher extent of degradation during the process. However, it could be noticed that all materials allowed the preparation of non-brittle self-standing films. The TGA thermograms relative to the nanocomposites (Supplementary Fig. 1) exhibit degradation temperatures comparable to the one of PLAref for low filler content. For high content of fillers, a lower $T_{d\ onset}$ value is obtained, with a minimum value of 337 °C for PLA/HNT/10 (Table 3). The values of the residue measured at high temperature are in good agreement with the expected filler contents.

The DSC thermograms of the different nanocomposite series are given in Supplementary Fig. 2. The glass transition temperature values are comparable for PLA ref and the different nanocomposites except for, PLA/OMMT/10 and PLA/OMMT/15 which exhibit a slightly lower T_g, value (around 50 °C) (Table 4). Considering experimental uncertainties, it can be seen that introducing nanofillers in the PLA matrix does not induce significant modifications of the mobile amorphous fraction (MAF) and the rigid amorphous fraction (RAF) (Table 4). It appears then that for the nanocomposite's series investigated, the fillers have no effect on the polymer chain mobility. For the nanocomposites prepared with the highest amount of OMMT, the decrease of T_g could be related to the decrease of the PLA molar mass observed by SEC. The introduction of nanofillers has no effect on the cold crystallization temperature and the melting temperature. Furthermore, the degree of crystallinity is less than 4 ± 2 % meaning that all nanocomposites can be considered as mostly amorphous.

To conclude, the matrix microstructure and chain mobility of the nanocomposite films prepared by melt-blending are not significantly affected by the fillers. As a result, the permeability properties of the nanocomposites will depend more specifically on the dispersion state, content and shape of the incorporated fillers.

The dispersion state of the fillers for the different nanocomposites films has been investigated by TEM. Moreover, to go deeper in the filler dispersion study, quantitative analysis has been realized through quantitative parameters such as the mean size, mean aspect ratio of the dispersed domains and the average density of the filler domains. As shown in Fig. 4, for PLA filled with silica, a good dispersion made of small aggregates is observed whatever the silica type and content up to 10 vol%. In complement of Fig. 4, TEM micrographs at low magnification are available in supplementary material (Supplementary Fig. 3 and Supplementary Fig. 5). TEM micrographs with the area distribution for the whole range of PLA/silica nanocomposite compositions are given in Supplementary Fig. 4 for hydrophilic silica and in Supplementary Fig. 6 for hydrophobic silica.

Table 5 gives the values of the mean area of the silica domains, the mean aspect ratio, the number of domains per unit surface and the distance between the silica domains. It can be remarked that, at similar filler content, the mean size of the aggregates is larger for hydrophilic silica (PLA/SiOH) than for hydrophobic silica (PLA/$SiCH_3$). This trend has also been reported in the literature when comparing surface-modified and non-modified silica in PLA [35,36] and explained by a difference in the filler/matrix compatibility which depends on the filler surface properties. The average silica domains area increases with increasing filler content for hydrophilic silica contrary to hydrophobic silica for which the domain area does not vary at filler contents below

Table 4
Matrix properties of the different nanocomposite films.

Sample	$T_{g\ onset}$ (°C)	$T_{cc\ onset}$ (°C)	T_m (°C)	χ_c (%)	$\Delta C_{p\ Tg}$ (J. $g^{-1}°C^{-1}$)	MAF (%)	RAF (%)
PLAref	57 ± 1	103 ± 1	150 ± 2	0 ± 2	0.52 ± 0.02	100 ± 4	0 ± 6
PLA/SiOH/1	57 ± 1	102 ± 1	149 ± 1	1 ± 2	0.51 ± 0.01	99 ± 5	0 ± 7
PLA/SiOH/3	57 ± 1	103 ± 1	149 ± 1	2 ± 2	0.49 ± 0.01	99 ± 5	0 ± 7
PLA/SiOH/4	57 ± 1	102 ± 1	149 ± 1	3 ± 2	0.43 ± 0.01	88 ± 5	9 ± 7
PLA/$SiCH_3$/1	56 ± 1	101 ± 1	149 ± 1	1 ± 2	0.49 ± 0.01	96 ± 5	3 ± 7
PLA/$SiCH_3$/4	56 ± 1	104 ± 1	149 ± 1	2 ± 2	0.48 ± 0.02	99 ± 5	0 ± 7
PLA/$SiCH_3$/5	56 ± 1	104 ± 1	149 ± 1	2 ± 2	0.48 ± 0.02	100 ± 5	0 ± 7
PLA/$SiCH_3$/10	56 ± 1	110 ± 1	150 ± 1	4 ± 2	0.40 ± 0.02	92 ± 6	4 ± 8
PLA/Ag/0.5	56 ± 1	103 ± 1	149 ± 1	1 ± 2	0.50 ± 0.02	100 ± 4	0 ± 6
PLA/Ag/1	55 ± 1	102 ± 1	149 ± 1	3 ± 2	0.50 ± 0.02	100 ± 5	0 ± 7
PLA/Ag/3	54 ± 1	101 ± 1	148 ± 1	2 ± 2	0.42 ± 0.02	100 ± 6	0 ± 8
PLA/Ag/4	53 ± 1	101 ± 1	148 ± 1	2 ± 2	0.36 ± 0.02	95 ± 6	3 ± 8
PLA/HNT/0.5	55 ± 1	102 ± 1	149 ± 1	0 ± 2	0.53 ± 0.01	100 ± 4	0 ± 6
PLA/HNT/2	55 ± 1	109 ± 1	151 ± 1	0 ± 2	0.48 ± 0.01	96 ± 5	4 ± 7
PLA/HNT/4	54 ± 1	109 ± 1	152 ± 1	1 ± 2	0.49 ± 0.01	100 ± 5	0 ± 7
PLA/HNT/10	55 ± 1	108 ± 1	150 ± 1	3 ± 2	0.38 ± 0.01	90 ± 6	7 ± 8
PLA/OMMT/2.5	56 ± 1	104 ± 1	149 ± 1	2 ± 2	0.52 ± 0.01	100 ± 4	0 ± 6
PLA/OMMT/5	55 ± 1	109 ± 1	150 ± 1	4 ± 2	0.48 ± 0.03	99 ± 4	0 ± 6
PLA/OMMT/10	52 ± 1	109 ± 1	151 ± 1	4 ± 2	0.42 ± 0.02	91 ± 4	5 ± 6
PLA/OMMT/15	50 ± 1	110 ± 1	151 ± 1	3 ± 2	0.38 ± 0.02	93 ± 5	7 ± 7
PLA/GNP/0.05	56 ± 1	102 ± 1	149 ± 1	3 ± 2	0.50 ± 0.02	96 ± 4	1 ± 6
PLA/GNP/0.1	58 ± 1	102 ± 1	149 ± 1	1 ± 2	0.52 ± 0.02	100 ± 4	0 ± 6
PLA/GNP/0.5	57 ± 1	102 ± 1	149 ± 1	1 ± 2	0.55 ± 0.02	100 ± 4	0 ± 6
PLA/GNP/1.5	56 ± 1	104 ± 1	150 ± 1	3 ± 2	0.49 ± 0.02	98 ± 4	0 ± 6

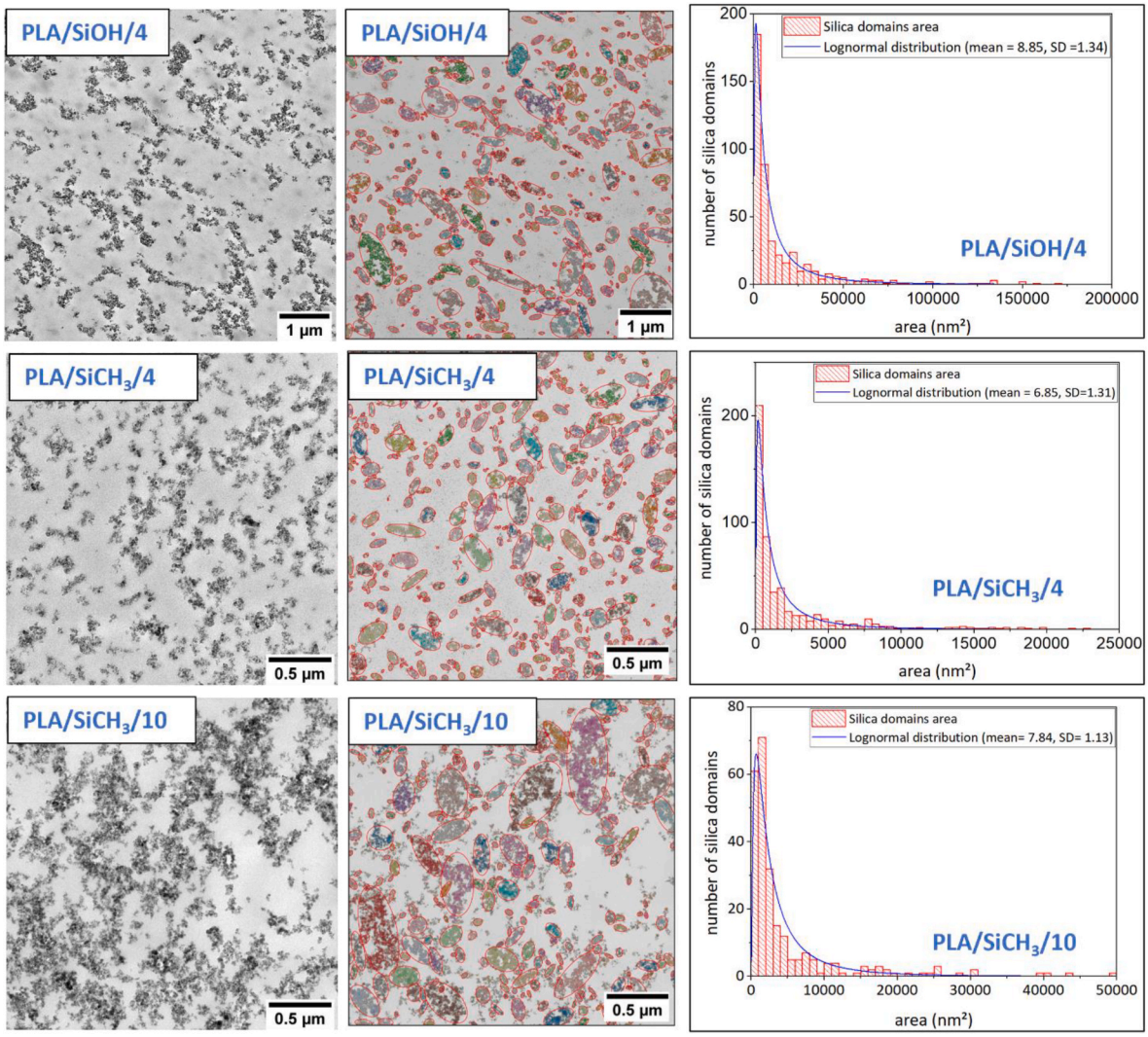

Fig. 4. TEM micrographs from the cross section of PLA/silica films and the silica domains identifications by Scikit-image processing and their area distribution for PLA/SiOH/4, PLA/$SiCH_3$/4 and PLA/$SiCH_3$/10.

10 vol%. However, the mean aspect ratio is the same in all the PLA/silica samples, with a value close to 2. It can be seen that there are more silica domains per surface unity for hydrophobic silica than for hydrophilic silica at similar filler content which shows again a better dispersion of the hydrophobic silica in PLA and logically the distance between the silica domains is smaller in these nanocomposites. At 10 vol%, PLA filled with hydrophobic silica (PLA/$SiCH_3$/10) shows less domains but bigger ones caused by the rather high amount of fillers which prevents a fine dispersion of silica and favours aggregation phenomena.

For the nanocomposites based on silver nanoparticles, a heterogeneous filler dispersion is evidenced, with the coexistence of single silver fillers and micrometer size agglomerates (Fig. 5 and Supplementary Fig. 7). Therefore, it has been decided to calculate the area as well as the aspect ratio values by separating the small domains with a diameter below 1 μm and the bigger domains (diameter >1 μm). Nevertheless, it can be noted that the proportion of micrometer domains is very low (<10 %) for all the silver contents (Table 6). The average area of the small domains keeps constant for all the samples with a mean value of 5.10^4 nm^2, whereas the size of the bigger domains increases by one decade between PLA/Ag/0.5 and PLA/Ag/4. Despite these differences of area, the mean aspect ratio is approximately equal to 1.7 in all the samples. Moreover, the mean number of domains is increasing with the silver content from 3 to 16 domains/μm^2 and the interdomains spacing decreases with the filler content but stays very large (>1,000 nm).

Halloysite nanotubes are well dispersed within the matrix, which may show a rather good compatibility of the tubes with the PLA matrix. Indeed, the TEM images representative of the film cross section of PLA/HNT/4 show the presence of few small discs, the size of which corresponds to the diameter of the tubes (Fig. 6a). This observation is confirmed by additional TEM micrographs in supplementary material (Supplementary Fig. 8). Few elongated structures are also evidenced corresponding to the length of unitary tubes. Therefore, it seems that most of the tubes are lying in the plane of the film. The top view of the same sample shown in Fig. 6b supports the conclusion drawn from the analysis of the cross sections. Indeed, it shows mostly elongated shapes corresponding to individual tubes lying parallel to the top view. This orientation of the tubes, lying parallel to the surface of the films can be generalized for all the halloysite contents. From these pictures, the length over diameter ratio of the observed individual tubes has been estimated equal to 10 which is in good agreement with the data relative to the individual fillers (Table 1). Increasing the filler amount up to 10 % vol leads to the presence of more numerous small aggregates (Fig. 6c), which is in agreement with results reported in other studies on PLA/HNT nanocomposites prepared by melt-blending [12,13,21].

Although the diameter of these aggregated structures measured on TEM pictures of the cross section is between 200 and 500 nm which is much larger than individual tubes (d ≈ 40 nm) their proportion is low (<10 %) whatever the halloysite content (Table 7). Consequently, the

Table 5
– Area, mean aspect ratio, average number of silica domains per unit surface and distance between the impermeable domains for PLA nanocomposites filled with hydrophilic silica (PLA/SiOH) and hydrophobic silica (PLA/$SiCH_3$).

Sample	Area (nm^2)	Mean aspect ratio	Number of domains/μm^2	Inter domains spacing (nm)
PLA/SiOH/1	9 000 ± 7 000	1.7 ± 0.5	5	550 ± 200
PLA/SiOH/3	18 000 ± 30 000	1.8 ± 0.6	7	430 ± 130
PLA/SiOH/4	20 000 ± 30 000	1.8 ± 0.7	16	380 ± 160
PLA/$SiCH_3$/1	3 000 ± 3 000	1.9 ± 0.5	12	290 ± 100
PLA/$SiCH_3$/4	3 000 ± 3 000	1.9 ± 0.6	70	120 ± 40
PLA $SiCH_3$/5	3 000 ± 5 000	1.9 ± 0.7	60	140 ± 40
PLA/$SiCH_3$/10	8 000 ± 10 000	1.9 ± 0.7	20	150 ± 60

mean L/D ratio of the halloysites domains in all the samples has been considered to be 10 (reflecting thus the presence of a great majority of individual tubes). From the results in Tables 7 it can be seen that the interparticle spacing decreases by a factor of 4 as the filler content increases from PLA/HNT/0.5 to PLA/HNT/10.

Fig. 7 shows representative TEM micrographs of PLA filled with Cloisite® 30B. Additional TEM images at higher magnification are presented in supporting material (Supplementary Fig. 9). A homogeneous dispersion of the randomly oriented fillers with the co-existence of quasi-individual sheets, small and middle size tactoïds for all filler contents up to 15 vol% is evidenced as already described in the literature [6,7,37]. This homogeneous dispersion is promoted by the presence of hydroxyl functions on the organic cation of the Cloisite® 30B [21].

The quantitative analysis of the filler dispersion state (Table 8) shows that the proportion of quasi-individual sheets is slightly decreasing as the filler content increases (from 84 % for PLA/OMMT/2.5 to 78 % for PLA/OMMT/15) due the hindrance which is not favorable to fine dispersion of the fillers [16]. This leads to an increase of the proportion of middle-size tactoïds with the filler content whereas the proportion of small tactoïds stays constant until 10 %vol of filler. For 15 vol% of OMMT, the proportion of small and middle size tactoïds is higher and the presence of micron size agglomerates has also been observed although present in very small amount. It is worth noting that the mean aspect ratio stays similar whatever the filler amount, in the range between 79 and 86, which is higher than the mean value of 60 calculated by Tenn et al. [7]. Moreover, the lamellar fillers are randomly oriented in all nanocomposite films. However, it should be noted that it is not always the case in films prepared by melt-blending. While, Tenn et al. [7] also reported a random orientation of the lamellae, other authors ([6,21]) have observed an orientation of the lamellae parallel to the surface of the films. Finally, it can be noted that the interdomains spacing is very small and decreases slightly as the montmorillonite content increases.

Dispersion of graphene was also investigated and TEM micrographs are shown in Fig. 8. At low GNP content (≤0.1 vol%), very good dispersion has been achieved with only few small stacks visible at low magnification. A lot of individual sheets are lying parallel to the surface of the films and it can be observed that the sheets can overlap horizontally and form elongated thin structures (Fig. 8). The length of these overlapped structures has been measured and is in a range between 1000 and 1500 nm. Thus, it leads to impermeable domains with higher aspect ratio than the individual graphene sheets. The lack of contrast as well as the few numbers of sheets due to the very low volume content of GNP did not allow to make a statistical analysis of the dispersion as for the other fillers. At higher GNP content (>0.1 vol%), TEM micrographs at low magnification show more numerous and bigger stacked sheets, with a mean aspect ratio of 5; their proportion increases which the GNP

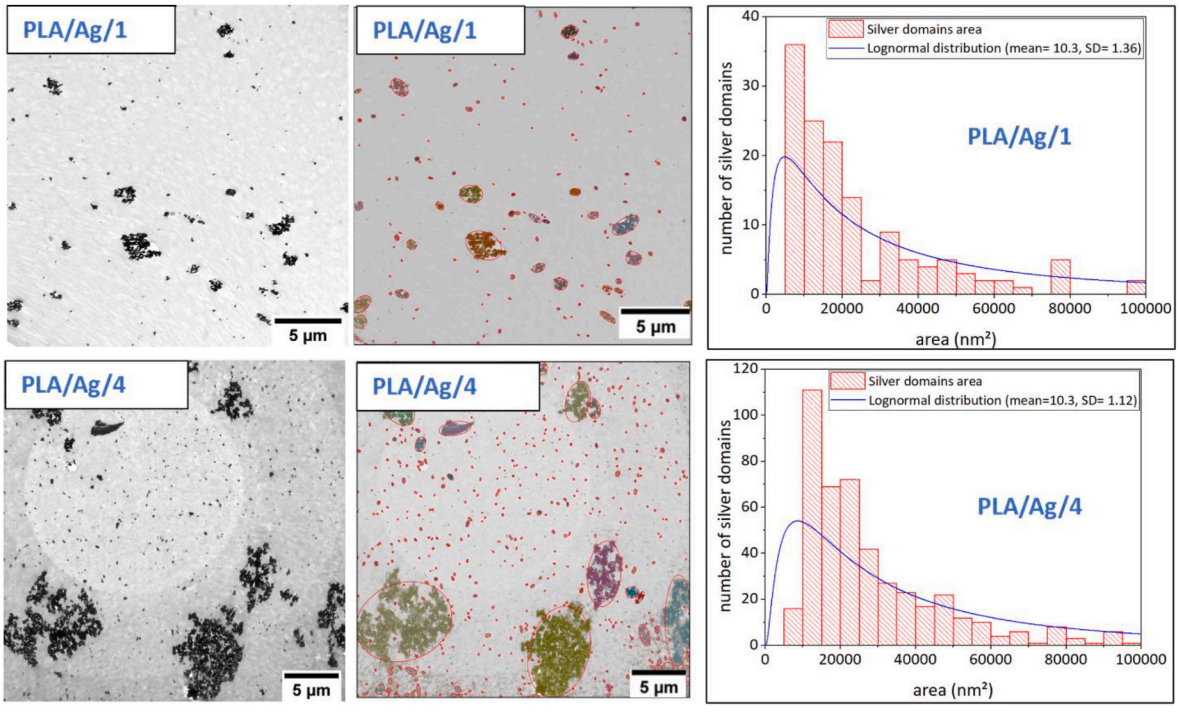

Fig. 5. TEM micrographs from the cross section of PLA/silver films as well as the silver domains identification by Scikit-image processing and their area distribution for PLA/Ag/1 and PLA/Ag/4.

Table 6
Area, mean aspect ratio, average number of silver domains per surface unity and distance between the impermeable domains for PLA nanocomposites filled with silver nanoparticles (PLA/Ag).

Sample	*Small domains ($d < 1$ µm)*			*Big domains ($d > 1$ µm)*			*All the domains*		
	% by number	Area (nm^2)	Aspect ratio	% by number	Area	Aspect ratio	Mean aspect ratio	Number of domains/ μm^2	Inter domains spacing (nm)
PLA/Ag/ 0.5	97	$(5 \pm 9).10^4$	1.7	3	$(5 \pm 2).10^5$	1.4	1.7	3	4,000 ± 2,000
PLA/Ag/1	92	$(5 \pm 7).10^4$	1.7	8	$(9 \pm 7).10^5$	1.7	1.7	7	2,000 ± 800
PLA/Ag/3	94	$(4 \pm 5).10^4$	1.6	6	$(3 \pm 6).10^6$	2.1	1.6	13	1,200 ± 600
PLA/Ag/4	95	$(4 \pm 3).10^4$	1.6	5	$(5 \pm 9).10^6$	1.9	1.6	16	1,200 ± 600

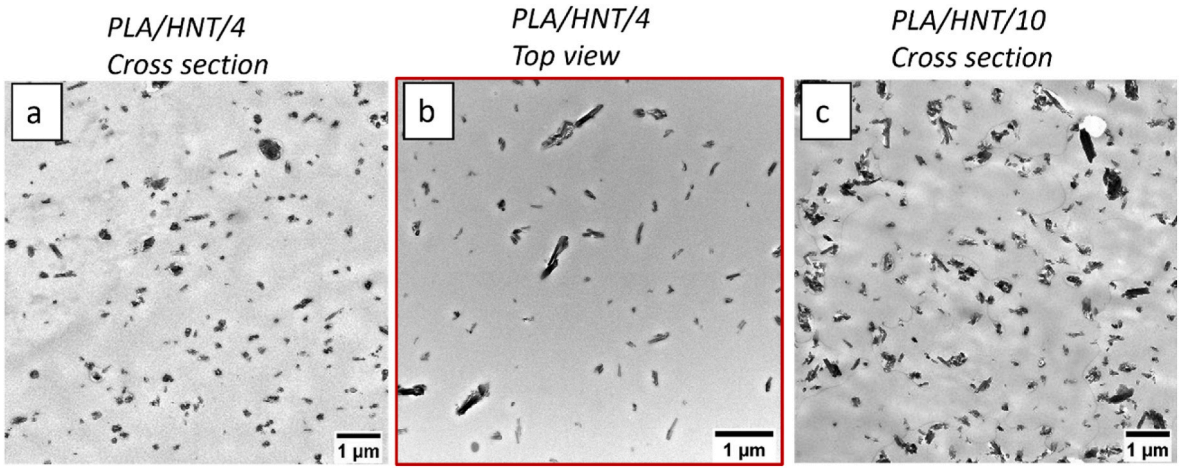

Fig. 6. TEM micrographs of (a) PLA/HNT/4 from the cross section, (b) PLA/HNT/4 from the top view and (c) PLA/HNT/10.

Table 7
Proportion of aggregated nanotubes domains and their diameter as well as the interdomains spacing values calculated from TEM pictures for halloysites nanocomposites (PLA/HNT).

Sample	% aggregated domains	Aggregates diameter (nm)	Inter domains spacing (nm)
PLA/HNT/ 0.5	3	450 ± 50	2130 ± 400
PLA/HNT/ 2	4	490 ± 220	1300 ± 500
PLA/HNT/ 4	3	250 ± 80	510 ± 170
PLA/HNT/ 10	10	320 ± 120	540 ± 160

content. The TEM micrographs at higher magnification for PLA/GNP/0.5 (Fig. 8) also show denser tactoïds. Consequently, it leads to a decrease of the mean filler aspect ratio.

To sum up, different dispersion states have been evidenced as a function of the type of fillers going from very homogeneous dispersion with silica to more heterogeneous ones with silver. The shape and the mean aspect ratio of the dispersed domains also vary according to the different systems with low elongated impermeable domains for PLA filled with silica (PLA/$SiCH_3$ and PLA/SiOH) in comparison to lamellar domains with high aspect ratio for PLA filled with montmorillonites (PLA/OMMT) or graphene (PLA/GNP). Moreover, the mean distance between the impermeable domains also varies a lot depending on the samples, with very close domains for PLA/OMMT and PLA/GNP to rather distant ones for PLA/Ag and PLA/HNT. Finally, the wide range of nanocomposites enables to have a wide range of dispersion state, content and shape of incorporated fillers.

3.2. Semi-crystalline PLA films

Another type of impermeable phase has been considered in this work: the polymer crystalline phase. To vary the extent of crystallinity, different annealing conditions were applied to the amorphous PLA reference film. The annealing temperatures were fixed at 110 and 120 °C from previous detailed studies focused on crystallization for the PLA commercial grade used in the present work [6,10].

3.2.1. Crystalline morphology

The evolution of the degree of crystallinity as a function of the annealing time for isothermal crystallization performed at $T_a = 110$ °C and $T_a = 120$ °C is reported in Fig. 9. A sharp increase of the crystallinity from 0 to 35 % is observed for an annealing time between 3 and 10 min, and then the degree of crystallinity increases more slowly until 24 h (1440 min) of annealing, to reach a maximum: $\chi_c = 50$ %. Similar curve shape has already been described in the literature ([25–27]) and the smoother slope after 10 min is attributed to a perfection of the crystalline structure also referred as secondary crystallization. Spherulites were evidenced by SEM observations performed on etched semi-crystalline PLA films (Fig. 10), which is common for crystallization without any mechanical constraint. Regardless of the degree of crystallinity and the annealing temperature, spherulites were found to be very small, with a diameter in the range of 1–2 µm. The spherulite size observed in our samples is slightly smaller than those that have been reported in the literature for similar annealing temperatures (around 5–10 µm) [24,25,27]. As the degree of crystallinity increases, the distance between the spherulites decreases until they completely fill the space as it can be seen in Fig. 10.

The DSC thermograms of PLA membranes annealed at $T_a = 110$ °C (Fig. 11a) show the presence of two melting peaks for short annealing

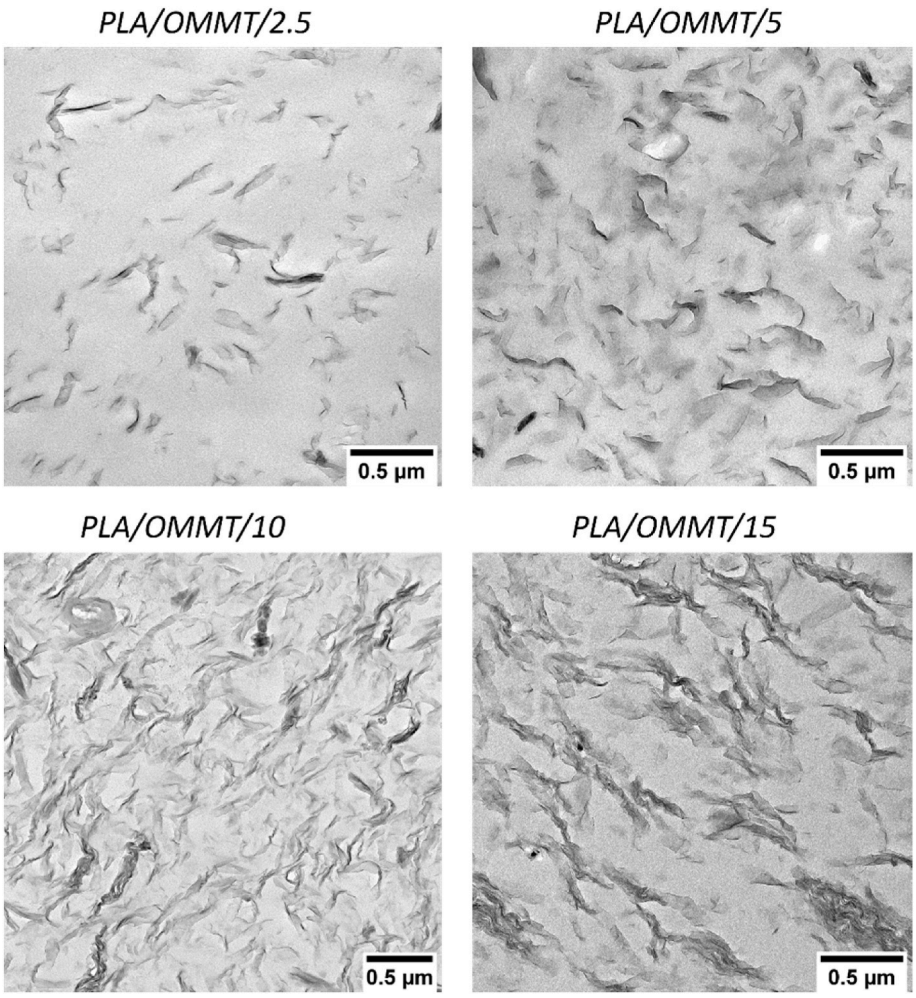

Fig. 7. TEM micrographs of the cross section of the PLA films filled with increasing amount of OMMT.

Table 8
Characteristics of the OMMT dispersion in the PLA/OMMT films. (w stands for the thickness of the filler domains).

Sample	*quasi-individual sheets*		*Small tactoïds (w < 30 nm)*		*Middle size tactoïds (30 <w < 200 nm)*		*Micron size agglomerates (w > 200 nm)*		*Mean aspect ratio*	*Interdomains spacing (nm)*
	% by number	Aspect ratio	% by number	Aspect ratio	% by number	Aspect ratio	% by number	Aspect ratio		
PLA/OMMT/2.5	84	100	10	12 ± 5	6	7 ± 2	/	/	86	190 ± 100
PLA/OMMT/5	85	100	10	10 ± 2	6	5 ± 2	/	/	86	150 ± 60
PLA/OMMT/10	80	100	10	10 ± 2	10	7 ± 2	/	/	83	60 ± 30
PLA/OMMT/15	78	100	5	7 ± 2	14	7 ± 2	3	2 ± 1	79	100 ± 30

time until 30 min, while there is only one melting peak for longer annealing time. For samples annealed at 120 °C the presence of two melting peaks becomes less noticeable (Fig. 11b). These observations are consistent with previous studies with the same D-isomer content as our PLA and the same annealing temperature used in this study [38,39]. In the literature, this double peak is attributed the melt-recrystallisation-melt process upon heating of the imperfect or less stable crystals [38]. Moreover, the DSC thermograms obtained for annealing at 110 °C and 120 °C demonstrate a slight shift in the melting temperature from 147 °C to 154 °C with increasing annealing time. This can be related to the increase of the thickness of the crystalline lamellae.

WAXS measurements were carried out on PLA samples with different degrees of crystallinity. Fig. 12 exhibits the diffractograms obtained and the assignment of the diffraction peaks. All semi-crystalline samples exhibit reflection peaks associated to the α crystalline form of PLLA which is commonly obtained for the used crystallization conditions [24], [39], [40], (200) and (203) planes at $2\theta = 16.8°$ and 19.0°, with an increase of the peak intensities when χ_c increases. It can also be remarked that for $\chi_c > 35$ %, small reflection peaks related to (004)/(103), (204) and (015) planes appear at $2\theta = 12.5°$, 20.6° and 22.3°, respectively; they are also characteristic of the α crystalline form of PLLA [41–43]. Finally, the α form is confirmed by the presence of small reflection peaks at $2\theta = 23.9°$ and at $2\theta = 25°$, associated to the (016) and (206) planes [40].

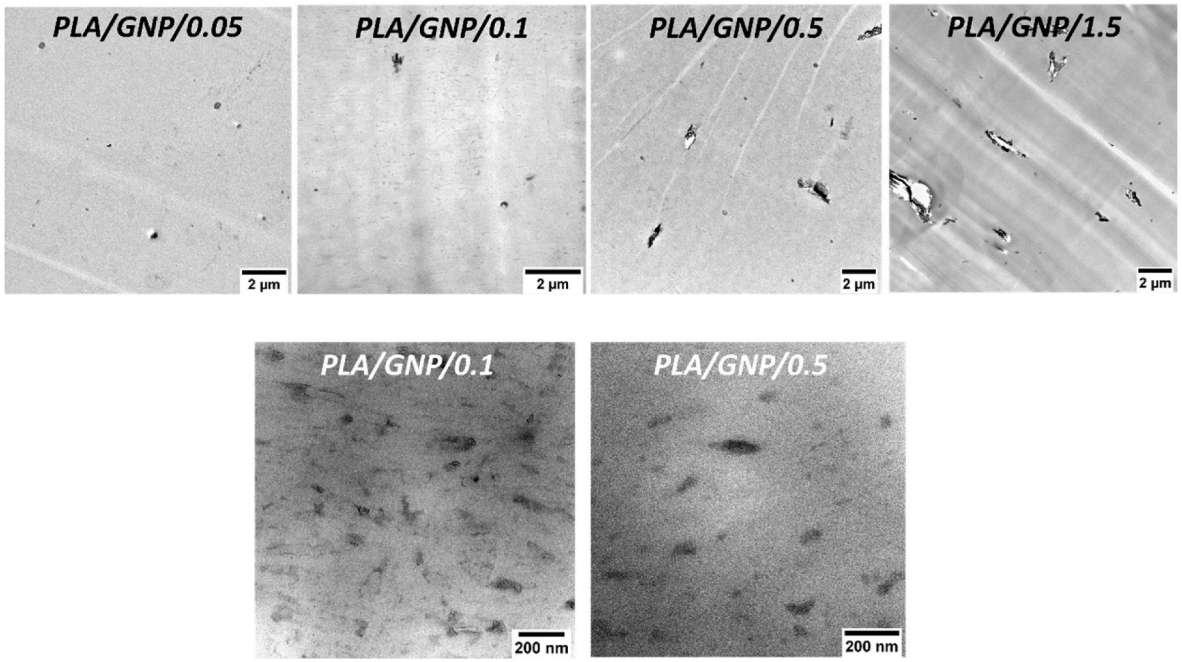

Fig. 8. TEM micrographs of the cross section of the PLA films filled with graphene at low (up) and high magnification (down).

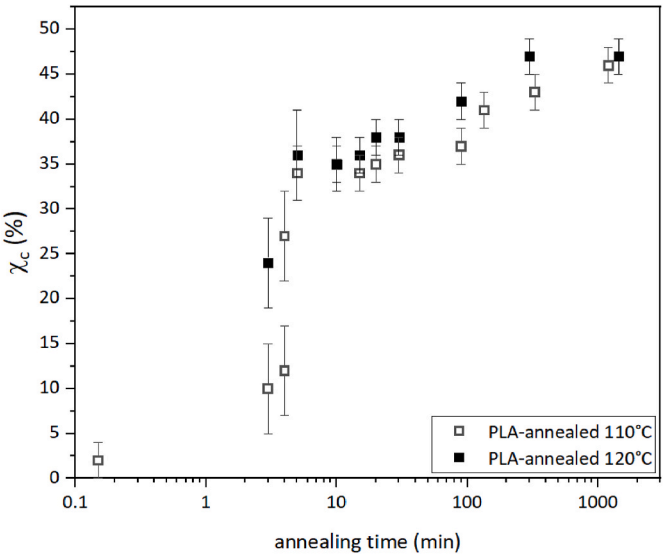

Fig. 9. Evolution of the crystallinity of the PLA film as a function of the annealing time (log scale) during isothermal crystallization at 110 °C and 120 °C.

SAXS analyses were also performed on annealed PLA with different degree of crystallinity (Fig. 13). The Lorentz-corrected scattering diagrams $I(q).q^2 = f(q)$ are represented in Fig. 13a. Except for PLA ref, all samples present a scattering intensity with a maximum obtained at a scattering wavevector q_{max}. The values of q_{max} are obtained after fitting with a Lorentz function; they are related to the long period values, L_p, which were calculated according to Bragg's law [27].

$$L_p = \frac{2\pi}{q_{max}} \tag{5}$$

From L_p, the crystalline lamellae thickness (L_c) and the thickness of the intercrystallite amorphous region (L_a) were calculated by using Equations (6) and (7).

$$L_c = L_p.\chi_c \tag{6}$$

$$L_a = L_p - L_c \tag{7}$$

Fig. 13b shows the evolution of the long period (L_p), the crystalline lamellae thickness (L_c) and the distance between the crystalline lamellae (L_a) as a function of χ_c. L_p values decrease from 24 to 20 nm for χ_c between 11 % and 35 % and then reach a plateau with a value of 20 nm, which is in agreement with literature data reported for PLA [26]. The crystalline lamellae thickness (L_c) increases from 2.5 nm to 10 nm with χ_c, while the distance between them (L_a) decreases from 20 nm to 10 nm. This increase of the L_c value is related with the shift towards higher temperature of the melting temperature. For $\chi_c = 50$ %, L_c value is equal to the L_a value (i.e. 10 nm) which is similar to values reported in the literature [26]. Moreover, similar value of L_p and L_c have been reported at $\chi_c = 35$ % independently of the annealing temperature, e.g. 110 or 120 °C [10].

3.2.2. *Structural description of the amorphous phase*

The modulated DSC thermogram of the annealed PLA is given in Supplementary Fig. 10. For all semi-crystalline PLA samples, the T_g value is 55 °C. No significant T_g shift was observed when comparing the reference amorphous PLA films and the annealed films which is consistent with the study of Guinault et al. [24]. Additionally, the amorphous phase contained in our semi-crystalline samples has also been investigated by taking an interest to the mobile amorphous fraction (*MAF*) and rigid amorphous fraction (*RAF*). The presence of a RAF in semi-cystalline PLA has been highlighted by several authors in the literature, which is due to the constraints imposed by the crystalline phase on the polymer chains of the amorphous phase [24–26]. Fig. 14a shows the evolution of the amount of RAF in the amorphous phase for different degrees of crystallinity investigated in this work. The RAF increases slowly as the degree of crystallinity increases from 2 % to 30 %. Above 30 % of crytallinity, the RAF increase is much more siginficant. Such an increase has also been reported both for PDLLA [44] and for PLLA annealed by a cold crystallization process [26,45,46]. In these studies, the strong increase of the RAF is explained by a decrease of the free volumes in the amorphous phase caused by annealing process as soon as the maximum of cristallinity is almost reached.

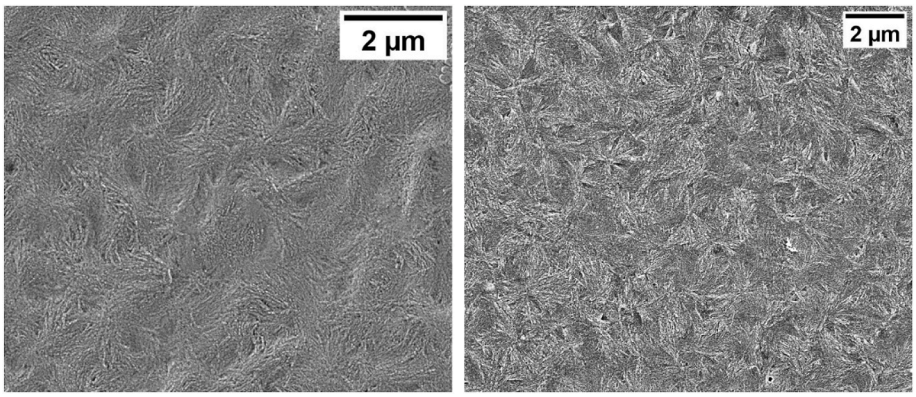

Fig. 10. SEM images (x10,000) of annealed PLA respectively for PLA/110 °C/11 and PLA/120 °C/50.

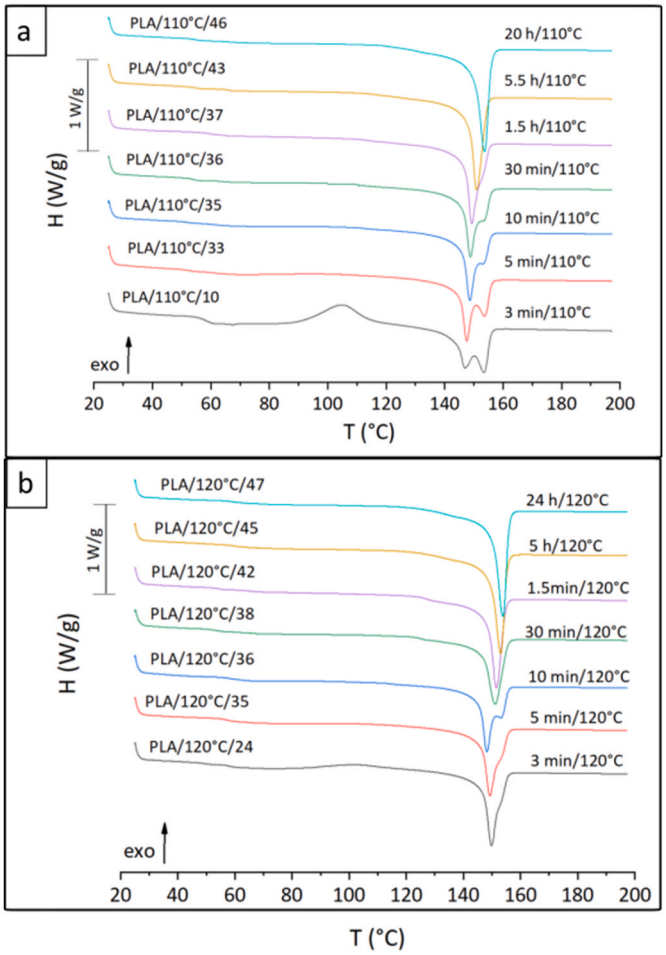

Fig. 11. DSC thermogram of annealed PLA films at a) 110 °C and b) 120 °C.

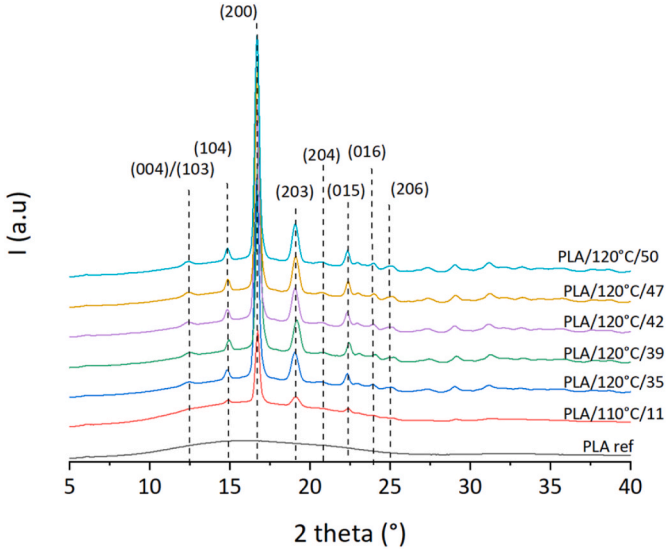

Fig. 12. WAXS patterns for semi-crystalline PLA with different degree of crystallinity.

The evolution of the RAF is also represented as a function of the distance between crystalline lamallae (L_a) in Fig. 14b. It can be observed that the proportion of *RAF* increases as L_a decreases, which is expected since the closer the lamellae, the greater the constraint on the chains of the amorphous phase and thus the lower the mobility is. However, the *RAF* content remains globally low (below 25 %), explaining the absence of a shift of the T_g [24].

All in all, annealing treatment of amorphous PLA at 110 and 120 °C shows the formation of a crystalline phase corresponding to the α-form of the PLA and organized into small (diameter ≈ 1 µm) spherulites. The increase of the degree of crystallinity leads to an increase of the crystalline lamellae thickness L_c as well as a decrease of the amorphous area thickness. Moreover, the increase of crystallinity has also consequences on the amorphous phase, with an increase of the rigid amorphous fraction (*RAF*) above 30 % of crystallinity.

3.3. Gas and water vapor permeability of amorphous nanocomposites and semi-crystalline PLA films

Oxygen permeability at anhydrous state and water vapor permeability at 90 %RH were measured at 23 °C on the different film series with two major aims. The first one is to evidence in each nanocomposite film series the factors governing transport properties. The second one is to establish equivalence laws for transport properties between the different series of nanocomposites investigated. The permeability coefficients measured for PLA reference, called P_0, are P_0 ($H_2O_{\ 90\ \%RH}$) = 3,600 barrer and P_0 ($O_{2\ 0\ \%\ RH}$) = 0.52 barrer. These permeability values are in the range of values reported in the literature for amorphous PLA [6,10,25,47–49].

The permeability coefficient, P, was then measured for the same diffusing molecule and conditions on each nanocomposite film and semi-crystalline film. The relative permeability was calculated for each penetrant and film series according to Equation (8):

$$Relative\ permeability = \frac{P}{P_0} \tag{8}$$

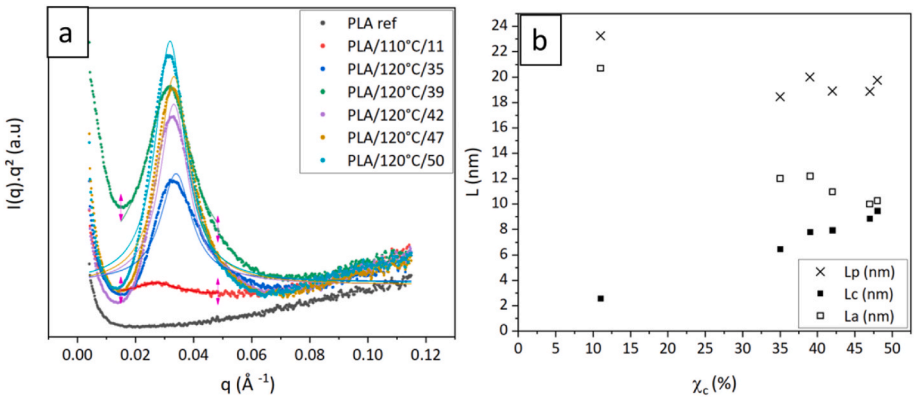

Fig. 13. a) SAXS scattering diagrams of semi-crystalline PLA for different degrees of crystallinity and the fitting with a Lorentz correction, (b) evolution of the long period (*Lp*), the crystalline lamellae thickness (*Lc*) and the intercrystallite amorphous thickness (La) as a function of the degree of crystallinity.

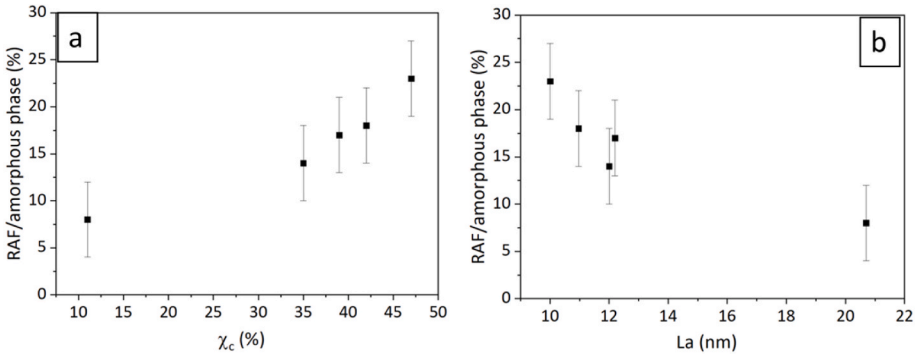

Fig. 14. (a) Evolution of the RAF as a function of crystallinity degree for PLA annealed at 120 °C and (b) as a function of the amorphous interlamellar distance.

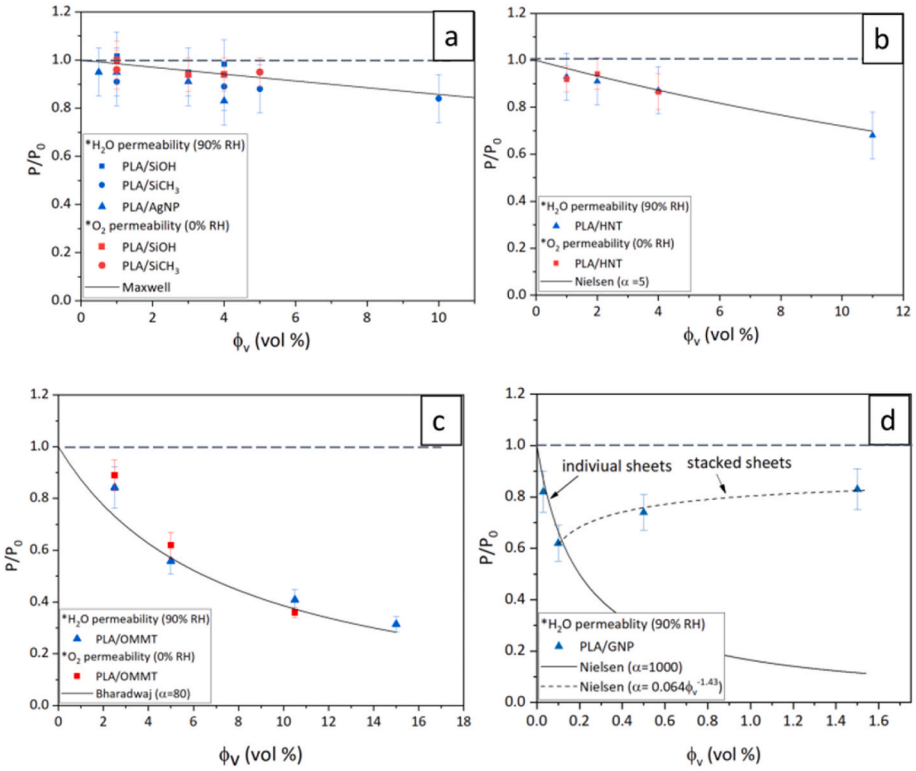

Fig. 15. Relative permeability as a function of the volume fraction of the different type of impermeable phase (a) spherical fillers, (b) halloysite nanotubes, (c) organo-modified montmorillonite and (d) graphene. Blue symbols stand for water vapor permeability and red symbols stand for dioxygen permeability. The dotted line (—) corresponds to a relative permeability of 1.

with P_0 the permeability of the reference PLA and P the permeability of the amorphous nanocomposite or semi-crystalline PLA sample.

First, it can be noticed that whatever the nanocomposite samples, the relative permeability is either below or equal to 1 (Fig. 15). Inorganic nanofillers such as those used in this work are considered as impermeable fillers [14,16,21] thus creating a tortuosity effect. In nanocomposites, the increase of the penetrant diffusion path and the decrease of the volume fraction of permeable phase are considered as the main factors at the origin of the permeability decrease. If the fraction of permeable phase depends on the filler volume fraction, the tortuosity depends on several factors: the initial filler shape, the filler volume amount, the filler dispersion state that is at the origin of the size and aspect ratio of the impermeable dispersed domains ([14,16]). Moreover, in the case of non-spherical domains, their orientation with respect to the gas diffusion path can also play a major role. As different nanofiller shapes were selected in our work, the relative permeability values of the nanocomposites are first discussed for each filler category. Table 9 summarizes the different models that have been used to describe the experimental results.

The relative permeability values for spherical fillers (silica and silver nanoparticles) are shown in Fig. 15a. Regardless of the diffusing molecule, i.e. O_2 or H_2O, all samples exhibit better barrier properties than the reference film. Moreover, considering the uncertainty on permeability values, all data define a single curve. The obtained relative permeability values are similar to those obtained by Morel et al. for calcium carbonate spherical nanoparticles (relative permeability around 0.95 for 4 vol% for nanofillers) [10]. It is noteworthy that the relative permeability values do not seem to depend on the nanofiller dispersion state as the fine dispersion of silica evidenced for PLA/SiOH/4 and PLA/$SiCH_3$/4 leads, for the same filler content, to similar relative permeability values as the silver aggregates observed for PLA/Ag/3 and PLA/Ag/4. It can then be concluded in the case of spherical fillers, that only the filler content is a discriminative parameter for barrier properties. Considering this conclusion, Maxwell model has been used to describe the evolution of relative permeability coefficients of the nanocomposite series based on spherical fillers. The Maxwell equation reported in Table 9 is commonly used for describing the evolution of relative permeability of nanocomposites polymers containing spherical impermeable fillers [10, 50–52]. The model provides permeability as a function of a single parameter: the content of impermeable phase volume (Φ_v) (Table 9). As shown by the solid line in Fig. 15a and the root mean square deviation (RMSD) value reported in Table 9, and considering experimental uncertainties, Maxwell model gives a good description of the relative permeability for the nanocomposite series based on hydrophilic silica, hydrophobic silica and silver.

Halloysite nanotubes (HNT) also lead to increased barrier properties as demonstrated in Fig. 15b. Here again, similar relative permeability decrease is obtained, regardless of the diffusing molecule, e.g. O_2 or H_2O. Compared to the study of Guo et al. [21], relative permeability values measured for our systems are slightly lower for a same halloysite content (e.g. 0.87 in our case for a halloysite content of 4 vol% compared to 0.98). Moreover, from the comparison of the data presented in Fig. 15 (a and b), it can be concluded that nanocomposites based on nanotubes exhibit superior barrier properties compared to nanocomposites based on spherical fillers. A previous work coupling experimental analyses and Finite Element Modeling on tubular based nanocomposites has underlined that the diffusion path in such systems could be viewed as resulting from both diffusion around the tube diameter and along the tube length, the first contribution being predominant [53]. Due to these two contributions, Maxwell law was inefficient to describe the permeability in such systems. On the other hand and as it was shown that halloysite tubes were mostly lying in the plane of the film, Nielsen model, which is usually used for nanocomposites containing platelets [6,14,54,55] could be appropriate. This model depends on the volume content as well as the mean aspect ratio (α) of the impermeable phase. The experimental relative permeability values obtained on the nanocomposites based on halloysite nanotubes were described with accuracy for an α value of 5 (Fig. 15) in agreement with the study of Htira et al. [53].

As shown in Fig. 15c, the use of organo-modified montmorillonites (Cloisite 30B) exhibits a significantly greater decrease in relative permeability as compared to spherical fillers and halloysite nanotubes. Extensive research in the literature has demonstrated the high efficiency of this type of filler in enhancing barrier properties ([2,8,9,56]), due to the high mean aspect ratio achieved when fine filler dispersion state was obtained (e.g. exfoliated or intercalated structures). Our morphological analysis has underlined that in our nanocomposites, the great majority of fillers are dispersed in the form of quasi-individual sheets with random orientation. It has also to be noticed that the relative permeability values measured are similar to those found in the literature for the same kind of systems [6,7]. Bharadwaj model [5] developed for modeling the barrier properties of nanocomposite with different possible orientation of platelet like fillers was chosen to fit the permeability behavior of PLA/OMMT nanocomposites. The value of the parameter S was fixed at 0 which reflects a random orientation of the fillers in the matrix as evidenced by microscopic observations. The fitting result is presented in Fig. 15c for an aspect ratio value (α) of 80, which corresponds to the mean aspect ratio calculated from our morphological analysis. As shown by the theoretical curve and the root mean square deviation (RMSD) value (Fig. 15c and Table 9), a good agreement is observed between experimental and calculated values.

The addition of graphene in the PLA matrix leads to a non-monotonous evolution of the relative permeability as a function of the filler amount. Indeed Fig. 15d shows a sharp decrease of the relative permeability below 0.1 vol% GNP leading to a relative permeability value of 0.62 for 0.1 vol% of graphene. For this low GNP content, by taking into account that the GNPs are lying in the film plane, a filler aspect ratio value (α) of 1000 is calculated from Nielsen laws. This aspect ratio value corresponds to that obtained from the microscopic observations. However, at higher GNP content (>0.1 vol%), the relative permeability increases with the GNP volume content. This behavior is different from the other filler types but not very surprising according to our morphological analysis which shows agglomerated sheets with low

Table 9
– Permeability models used in this work for the different types of impermeable phase.

Type of impermeable phase	Permeability model	Parameters value	RMSD
Spherical	***Maxwell model*** [59] $\frac{P}{P_0}=\frac{1-\phi_v}{1+\frac{1}{2}\phi_v}$	$\phi_v = 0-10\%$	*0.07 (calculated for PLA/$SiCH_3$)*
HNT nanotubes	***Nielsen model*** [54] $\frac{P}{P_0}=\frac{1-\phi_v}{1+\frac{\alpha}{2}\phi_v}$	$\phi_v = 0-10\%$ $\alpha = 5$	0.02
Organo-modified montmorillonite	***Bharadwaj model*** [5] $\frac{P}{P_0}=\frac{1-\phi_v}{1+\frac{\alpha}{2}\phi_v\frac{2}{3}\left(S+\frac{1}{2}\right)}$	$\phi_v = 0-15\%$ $\alpha = 80$ $S = 0$	0.06
Graphene	***Nielsen model*** [54] $\frac{P}{P_0}=\frac{1-\phi_v}{1+\frac{\alpha}{2}\phi_v}$	$\phi_v = 0-0.1\%$ $\alpha = 1000$ $\phi_v = 0.1-1.5\%$ $\alpha = 0.064\phi_v^{-1.43}$	/ /
Spherulites	***Michaels model*** [22], [23] $\frac{P}{P_0}=\frac{1-\chi_c}{\left(1+\frac{1}{2}\chi_c\right)\beta}$	$\beta = 1$ $\chi_c = 0-50\%$ $\beta = 1+\chi_c$ $\chi_c = 0-50\%$	0.11 0.06

Φv: filler content, α: aspect ratio, S: orientation parameter, β: chain immobilization factor, χc: degree of crystallinity.

aspect ratio. This behavior in "V" shape has already been reported in the literature in case of PLA filled with graphene [57,58]. For these GNP contents, the Nielsen model provides aspect ratio values of 140 and 25 for 0.5 vol% GNP and 1.5 vol% GNP, respectively which is in good agreement with microscopy observations. From these calculated aspect ratio values, Equation (9) was proposed to describe the evolution of the aspect ratio as a function of the GNP volume content for GNP >0.1 vol% (Fig. 16).

$$\alpha = 0.064\phi_v^{-1.43} \tag{9}$$

Combination of Equation (9) and Nielsen model allowed then to accurately describe the experimental relative permeability values above 0.1 vol% GNP (Fig. 15d).

These experimental results confirm, as expected, that the decrease of the relative permeability observed for nanocomposites highly depends on the amount and aspect ratio of the dispersed impermeable phase.

Except impermeable fillers, another type of phase which is organic can usually be considered as an impermeable phase. It is the crystalline phase in semi-crystalline polymers [22,24,60]. Fig. 17 confirms the improvement of barrier properties in annealed PLA by showing a significant decrease of the relative permeability as the degree of crystallinity increases. In addition, the permeability results remain unaffected by the annealing temperature due to the similarity in morphology. The results are consistent with previous studies on PDLLA films annealed at the same range of temperatures [6,24,25]. One aim of this work was to compare the effects of fillers and crystalline phase on the barrier properties. By comparing the results of Figs. 15 and 17, it can be observed that for the same amount of impermeable phase (10 vol%), P/P_0 (PLA/$SiCH_3$/10) > P/P_0 (PLA/110 °C/10) > P/P_0 (PLA/HNT/10) > P/P_0 (PLA/OMMT/10).

Thus, the crystalline phase leads to a higher permeability decrease than impermeable spheres and much lower than platelet like fillers. In fact, semi-crystalline polymers are complex systems in which coexist the amorphous permeable phase and the crystalline impermeable phase with polymer chains belonging to both phases. The morphology of the crystalline phase consists of crystalline lamellae whose size and aspect ratio can vary depending on the degree of crystallinity and processing conditions [24,25,61]. Literature based on modeling shows different trends concerning the effect of the crystallites size on barrier properties. According to Fricke model, the diffusion is more efficiently blocked in the case of wide and thin crystals [23]. However, Nilsson et al. [62] showed that in the case of spherulite type morphology, the size of the crystallites had no significant effect on the permeability. For our studied samples, crystallites are organized so that to form spherulites with amorphous phase in between the crystallites. Concerning, the amorphous phase, a particular attention has to be paid on the role of the interfacial area between crystallite and amorphous phase. As already discussed, polymer chains at the interface could be constrained leading to different chain mobility with respect to chains in the heart of the intercrystallite amorphous region. The *RAF* is representative of the amount of constrained amorphous phase. Different studies have investigated the role of *RAF* on the transport properties of annealed PLA and show that it has an influence of the permeability [24,25,46].

To go further in our analysis on the potential effect of *RAF*, a confrontation of experimental relative permeability values with calculated values from the two phases Michaels model [22,23] has been made (Equation (10)),

$$\frac{P}{P_0} = \frac{\phi_a}{\tau\beta} \tag{10}$$

In this model Φ_a is the amorphous fraction, τ the tortuosity factor. The authors showed that the β factor, which represents the immobilization of the amorphous chains by the crystallites, is equal to 1 for amorphous polymer and can increase more or less regularly when the fraction of amorphous phase decreases. Concerning the tortuosity factor, by making analogy between electrical conductivity and gas permeability it has been considered that for a spherulitic morphology, the tortuosity factor τ can be written according to Equation (11) [22]:

$$\tau = 1 + \frac{(1-\phi_a)}{2} \tag{11}$$

The relative permeability of our semi-crystalline systems has first been fitted with the Micheals model considering that $\beta = 1$ (Fig. 17). A non-negligible error is noted, especially for the higher degrees of crystallinity. Thus, to accurately fit the experimental data (RMSD = 0.06) the β factor was gradually increased from 1 for $\chi_c = 0$ % to 1.5 for $\chi_c =$ 50 % to reflect the decrease of the inter-lamellae spacing leading to the increase of the *RAF*.

Finally, thanks to the different models of permeability used to describe the experimental results in the most accurate way, an equivalence diagram has been built (Fig. 18) with the aim to make possible to compare the efficiency of the different fillers with respect to crystallinity in terms of barrier properties. The composition domain considered is the domain corresponding to fillers amount less than 15 vol% for which the

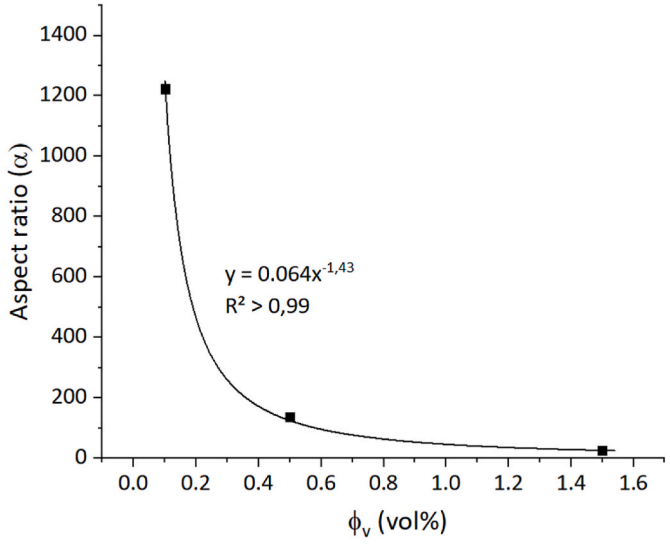

Fig. 16. Evolution of the theoretical aspect ratio (calculated form the Nielsen equation) with the graphene volume content.

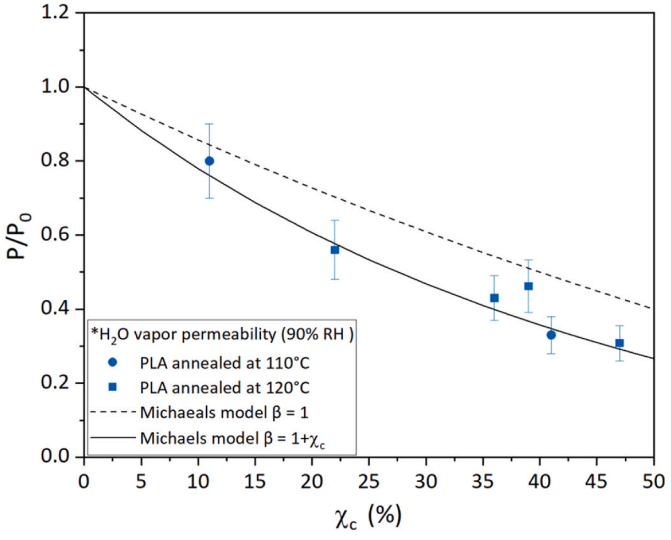

Fig. 17. Relative permeability as a function of the degree of crystallinity for annealed PLA at 110 °C and 120 °C.

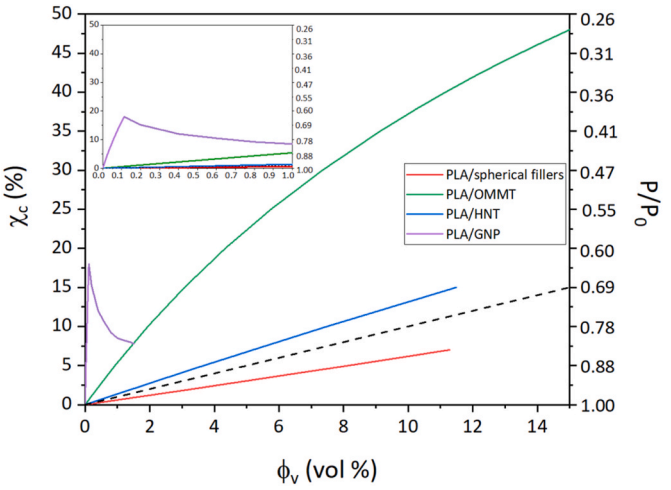

Fig. 18. Equivalence between the different types of fillers and the crystalline phase content in term of relative permeability. The dotted line represents theoretical perfect equivalence between the crystallinity and the fillers.

models could be validated by experimental data. In Fig. 18, the full lines represent the evolution of the relative permeability as a function of the volume amount of different filler types (spheres, tubes and platelets). The two Y axes directly show the impact of the crystallinity degree on the relative permeability. The dotted line represents a theoretical perfect equivalence between the crystallinity and the fillers. From the proposed representation, it can at first be seen that the curves relative to graphene, montmorillonite and halloysite are above the dotted line, showing a better efficiency of these fillers to reduce the permeability with respect to crystallinity. On the other hand, the curve relative to spherical fillers is below the dotted line. It is also easy to know the volume of each type of phase needed to achieve a given relative permeability value. For example, 8 %vol of crystalline phase would have the same efficiency on permeability than 0.05 vol% of GNP, 2 %vol of OMMT or 7.5 vol% of HNT or 15 vol% of spherical fillers. All these possibilities would lead to a relative permeability of 0.8.

4. Conclusion

In this work, PLA films containing different kinds of impermeable domains were prepared. Amorphous PLA nanocomposite films with different types of fillers (lamellae, spherical and nanotubes) were made by melt-blending and semi crystalline PLA were obtained by thermal treatments. The filler content ranged from 0 to 15 vol%, and crystallization degree up to 50 %.

Permeability of the films decreases whatever the type of impermeable phase, but different trends were observed. Thanks to in-depth analysis of samples microstructure, microstructure-permeability relations have been established. For the nanocomposite film series, the aspect ratio of the dispersed fillers is the most discriminant factor by increasing tortuosity effect. Consequently, for a same filler content, permeability of PLA filled with lamellar fillers was lower than spherical and tubular filler-based nanocomposites. Among the studied nanofillers, graphene led to the highest barrier properties with a relative permeability of 0.6 for 0.1 vol% but should be used at low amount due to aggregation phenomena observed as soon as 0.1 vol% of graphene. For semi-crystalline PLA, permeability decreased with the increase of crystallinity and the decrease of amorphous chain mobility.

Moreover, the detailed study of the microstructure in relation with permeability allowed to identify for each investigated materials series the governing factors and therefore to identify permeability models and their optimum parameters to accurately fit the experimental data. Finally, and for the first time, an equivalence between crystalline content and fillers content was established. In, this way the effect of each type of fillers (up to 15 vol%) on permeability and the equivalent crystallinity degree can be predicted.

CRediT authorship contribution statement

Aurore Jullin: Writing – original draft, Methodology, Investigation, Formal analysis, Data curation. **Guillaume Sudre:** Writing – review & editing, Formal analysis. **Nicolas Hascoët:** Writing – review & editing, Supervision. **Francisco Chinesta:** Writing – review & editing, Supervision. **Eliane Espuche:** Writing – review & editing, Validation, Supervision, Resources, Project administration, Methodology, Funding acquisition, Conceptualization.

Declaration of competing interest

The authors declare that they have no known competing financial interests or personal relationships that could have appeared to influence the work reported in this paper.

Acknowledgment

This work has been financially supported by the French National Research Agency (ANR) through BANCODEMM project. (ANR-21-CE06-0009-01) The authors gratefully acknowledge Fabrice Gouanvé for training on permeation equipment, Agnès Crépet for the chromatography experiments, Pierre Alcouffe and Eloi Chamczyck (Ingénierie des Matériaux Polymères, UMR CNRS 5223) and the Centre Technologique des Microstructures of University of Lyon 1 for SEM and TEM photomicrographs. The authors are also grateful to the European Synchrotron Radiation Facility (ESRF) and particularly Isabelle Morfin and Gilbert Chahine for assistance and support in using beamline BM02. The conducted experiments are under the number A02-1-925 (DOI:10.15151/ESRF-ES-1550904570). The Wide-angle X-ray detector (WOS) was funded by the French National Research Agency (ANR) under the "Investissement d'Avenir" program (Grant no. ANR-11-EQPX-0010).

Appendix A. Supplementary data

Supplementary data to this article can be found online at https://doi.org/10.1016/j.polymertesting.2024.108682.

Data availability

Data will be made available on request.

References

[1] Bioplastics market development update 2023, European Bioplastics e.V. https://www.european-bioplastics.org/market/, 2023. (Accessed 20 August 2024).
[2] S. Sinha Ray, K. Yamada, M. Okamoto, A. Ogami, K. Ueda, New polylactide/layered silicate nanocomposites. 3. High-performance biodegradable materials, Chem. Mater. 15 (2003) 1456–1465, https://doi.org/10.1021/cm020953r.
[3] J.-H. Chang, Y.U. An, G.S. Sur, Poly(lactic acid) nanocomposites with various organoclays. I. Thermomechanical properties, morphology, and gas permeability, J. Polym. Sci. B Polym. Phys. 41 (2003) 94–103, https://doi.org/10.1002/polb.10349.
[4] A.A. Arman Alim, S.S. Mohammad Shirajuddin, F.H. Anuar, A review of nonbiodegradable and biodegradable composites for food packaging application, J. Chem. 2022 (2022) 7670819, https://doi.org/10.1155/2022/7670819.
[5] R.K. Bharadwaj, Modeling the barrier properties of polymer-layered silicate nanocomposites, Macromolecules 34 (2001) 9189–9192, https://doi.org/10.1021/ma010780b.
[6] E. Picard, E. Espuche, R. Fulchiron, Effect of an organo-modified montmorillonite on PLA crystallization and gas barrier properties, Appl. Clay Sci. 53 (2011) 58–65, https://doi.org/10.1016/j.clay.2011.04.023.
[7] N. Tenn, N. Follain, J. Soulestin, R. Crétois, S. Bourbigot, S. Marais, Effect of nanoclay hydration on barrier properties of PLA/montmorillonite based nanocomposites, J. Phys. Chem. C 117 (2013) 12117–12135, https://doi.org/10.1021/jp401546t.

[8] S. Sinha Ray, K. Yamada, M. Okamoto, Y. Fujimoto, A. Ogami, K. Ueda, New polylactide/layered silicate nanocomposites. 5. Designing of materials with desired properties, Polymer 44 (2003) 6633–6646, https://doi.org/10.1016/j.polymer.2003.08.021.

[9] F. Li, C. Zhang, Y. Weng, Improvement of the gas barrier properties of PLA/OMMT films by regulating the interlayer spacing of OMMT and the crystallinity of PLA, ACS Omega 5 (2020) 18675–18684, https://doi.org/10.1021/acsomega.0c01405.

[10] F. Morel, E. Espuche, V. Bounor-Legaré, O. Persynn, M. Lacroix, Impact of coated calcium carbonate nanofillers and annealing treatments on the microstructure and gas barrier properties of poly(lactide) based nanocomposite films, J. Polym. Sci. B Polym. Phys. 54 (2016) 649–658, https://doi.org/10.1002/polb.23957.

[11] P. Cheviron, F. Gouanvé, E. Espuche, Effect of silver nanoparticles' generation routes on the morphology, oxygen, and water transport properties of starch nanocomposite films, J. Nanoparticle Res. 17 (2015) 364, https://doi.org/10.1007/s11051-015-3173-4.

[12] W.L. Tham, B.T. Poh, Z.A. Mohd Ishak, W.S. Chow, Transparent poly(lactic acid)/halloysite nanotube nanocomposites with improved oxygen barrier and antioxidant properties, J. Therm. Anal. Calorim. 126 (2016) 1331–1337, https://doi.org/10.1007/s10973-016-5834-7.

[13] G. Gorrasi, R. Pantani, M. Murariu, P. Dubois, PLA/Halloysite nanocomposite films: water vapor barrier properties and specific key characteristics, Macromol. Mater. Eng. 299 (2014) 104–115, https://doi.org/10.1002/mame.201200424.

[14] S. Singha, M.S. Hedenqvist, A review on barrier properties of poly(lactic acid)/clay nanocomposites, Polymers 12 (2020) 1095, https://doi.org/10.3390/polym12051095.

[15] E. Espuche, Nanocomposites for gas barrier applications: governing factors, single and coupled effects, new routes to optimise the function properties, Polym. Test. 125 (2023) 108124, https://doi.org/10.1016/j.polymertesting.2023.108124.

[16] E. Picard, A. Vermogen, J.-F. Gérard, E. Espuche, Barrier properties of nylon 6-montmorillonite nanocomposite membranes prepared by melt blending: influence of the clay content and dispersion state: consequences on modelling, J. Membr. Sci. 292 (2007) 133–144, https://doi.org/10.1016/j.memsci.2007.01.030.

[17] E. Picard, J.-F. Gérard, E. Espuche, Reinforcement of the gas barrier properties of polyethylene and polyamide through the nanocomposite approach: key factors and limitations, Oil Gas Sci. Technol. – Rev. IFP Energies Nouvelles 70 (2015) 237–249, https://doi.org/10.2516/ogst/2013145.

[18] O. Gain, E. Espuche, E. Pollet, M. Alexandre, Ph Dubois, Gas barrier properties of poly(ε-caprolactone)/clay nanocomposites: influence of the morphology and polymer/clay interactions, J. Polym. Sci. B Polym. Phys. 43 (2005) 205–214, https://doi.org/10.1002/polb.20316.

[19] J. Trifol, D. Plackett, C. Sillard, O. Hassager, A.E. Daugaard, J. Bras, P. Szabo, A comparison of partially acetylated nanocellulose, nanocrystalline cellulose, and nanoclay as fillers for high-performance polylactide nanocomposites, J. Appl. Polym. Sci. 133 (2016), https://doi.org/10.1002/app.43257.

[20] L. Petersson, K. Oksman, Biopolymer based nanocomposites: comparing layered silicates and microcrystalline cellulose as nanoreinforcement, Compos. Sci. Technol. 66 (2006) 2187–2196, https://doi.org/10.1016/j.compscitech.2005.12.010.

[21] Y. Guo, K. Yang, X. Zuo, Y. Xue, C. Marmorat, Y. Liu, C.-C. Chang, M. H. Rafailovich, Effects of clay platelets and natural nanotubes on mechanical properties and gas permeability of Poly (lactic acid) nanocomposites, Polymer 83 (2016) 246–259, https://doi.org/10.1016/j.polymer.2015.12.012.

[22] A.S. Michaels, R.B. Parker Jr., Sorption and flow of gases in polyethylene, J. Polym. Sci. 41 (1959) 53–71, https://doi.org/10.1002/pol.1959.1204113805.

[23] A.S. Michaels, H.J. Bixler, Flow of gases through polyethylene, J. Polym. Sci. 50 (1961) 413–439, https://doi.org/10.1002/pol.1961.1205015412.

[24] A. Guinault, C. Sollogoub, V. Ducruet, S. Domenek, Impact of crystallinity of poly (lactide) on helium and oxygen barrier properties, Eur. Polym. J. 48 (2012) 779–788, https://doi.org/10.1016/j.eurpolymj.2012.01.014.

[25] M. Drieskens, R. Peeters, J. Mullens, D. Franco, P.J. Lemstra, D.G. Hristova-Bogaerds, Structure versus properties relationship of poly(lactic acid). I. Effect of crystallinity on barrier properties: structure Vs. Barrier Properties of PLA, J. Polym. Sci. B Polym. Phys. 47 (2009) 2247–2258, https://doi.org/10.1002/polb.21822.

[26] N. Delpouve, A. Saiter, J.F. Mano, E. Dargent, Cooperative rearranging region size in semi-crystalline poly(l-lactic acid), Polymer 49 (2008) 3130–3135, https://doi.org/10.1016/j.polymer.2008.04.045.

[27] S. Fernandes Nassar, A. Guinault, N. Delpouve, V. Divry, V. Ducruet, C. Sollogoub, S. Domenek, Multi-scale analysis of the impact of polylactide morphology on gas barrier properties, Polymer 108 (2017) 163–172, https://doi.org/10.1016/j.polymer.2016.11.047.

[28] Evonick, Safety data sheet Aerosil®200. https://www.freemansupply.com/MSDS/Combined/Fillers/Aerosil200.pdf, 2019.

[29] Sigma Aldrich data sheet, n.d. https://www.sigmaaldrich.com/FR/fr/product/aldrich/685445?srsltid=AfmBOorv9MaIdomGyD-J0X2EMwB_4lyNXqgYzEvjKkOZpubT9Y5Je-rr.

[30] American element data sheet, n.d. https://www.americanelements.com/silver-nanoparticles-7440-22-4.

[31] Nanoshel LCC data sheet, n.d. https://pdf.indiamart.com/impdf/8456503491/SELLER-1385392/graphene-nano-powder.pdf.

[32] B. Kalb, A.J. Pennings, General crystallization behaviour of poly(l-lactic acid), Polymer 21 (1980) 607–612, https://doi.org/10.1016/0032-3861(80)90315-8.

[33] F.-D. Kopinke, M. Remmler, K. Mackenzie, M. Möder, O. Wachsen, Thermal decomposition of biodegradable polyesters—II. Poly(lactic acid), Polym. Degrad. Stabil. 53 (1996) 329–342, https://doi.org/10.1016/0141-3910(96)00102-4.

[34] X. Monnier, D. Cavallo, M.C. Righetti, M.L. Di Lorenzo, S. Marina, J. Martin, D. Cangialosi, Physical aging and glass transition of the rigid amorphous fraction in poly(l-lactic acid), Macromolecules 53 (2020) 8741–8750, https://doi.org/10.1021/acs.macromol.0c01182.

[35] S.-M. Lai, Y.-T. Hsieh, Preparation and properties of polylactic acid (PLA)/Silica nanocomposites, J. Macromol. Sci., Part B 55 (2016) 211–228, https://doi.org/10.1080/00222348.2016.1138179.

[36] J. Sepulveda, C. Villegas, A. Torres, E. Vargas, F. Rodriguez, S. Baltazar, A. Prada, A. Rojas, J. Romero, S. Faba, M.J. Galotto, Effect of functionalized silica nanoparticles on the mass transfer process in active PLA nanocomposite films obtained by supercritical impregnation for sustainable food packaging, J. Supercrit. Fluids 161 (2020) 104844, https://doi.org/10.1016/j.supflu.2020.104844.

[37] A. Vermogen, K. Masenelli-Varlot, R. Séguéla, J. Duchet-Rumeau, S. Boucard, P. Prele, Evaluation of the structure and dispersion in polymer-layered silicate nanocomposites, Macromolecules 38 (2005) 9661–9669, https://doi.org/10.1021/ma051249+.

[38] P. Song, G. Chen, Z. Wei, W. Zhang, J. Liang, Calorimetric analysis of the multiple melting behavior of melt-crystallized poly(l-lactic acid) with a low optical purity, J. Therm. Anal. Calorim. 111 (2013) 1507–1514, https://doi.org/10.1007/s10973-012-2502-4.

[39] Z. Wei, P. Song, C. Zhou, G. Chen, Y. Chang, J. Li, W. Zhang, J. Liang, Insight into the annealing peak and microstructural changes of poly(l-lactic acid) by annealing at elevated temperatures, Polymer 54 (2013) 3377–3384, https://doi.org/10.1016/j.polymer.2013.04.027.

[40] M. Cocca, M.L.D. Lorenzo, M. Malinconico, V. Frezza, Influence of crystal polymorphism on mechanical and barrier properties of poly(l-lactic acid), Eur. Polym. J. 47 (2011) 1073–1080, https://doi.org/10.1016/j.eurpolymj.2011.02.009.

[41] J. Zhang, K. Tashiro, H. Tsuji, A.J. Domb, Disorder-to-Order phase transition and multiple melting behavior of poly(l-lactide) investigated by simultaneous measurements of WAXD and DSC, Macromolecules 41 (2008) 1352–1357, https://doi.org/10.1021/ma0706071.

[42] P. Pan, W. Kai, B. Zhu, T. Dong, Y. Inoue, Polymorphous crystallization and multiple melting behavior of poly(l-lactide): molecular weight dependence, Macromolecules 40 (2007) 6898–6905, https://doi.org/10.1021/ma071258d.

[43] D. Brizzolara, H.-J. Cantow, K. Diederichs, E. Keller, A.J. Domb, Mechanism of the stereocomplex formation between enantiomeric poly(lactide)s, Macromolecules 29 (1996) 191–197, https://doi.org/10.1021/ma951144e.

[44] N. Delpouve, A. Saiter, E. Dargent, Rigid and mobile amorphous fractions in two poly(lactic acid). 8th World Congress of Chemical Engineering, Montreal, 2009.

[45] M. Arnoult, E. Dargent, J.F. Mano, Mobile amorphous phase fragility in semi-crystalline polymers: comparison of PET and PLLA, Polymer 48 (2007) 1012–1019, https://doi.org/10.1016/j.polymer.2006.12.053.

[46] A. Sangroniz, A. Chaos, M. Iriarte, J. del Río, J.-R. Sarasua, A. Etxeberria, Influence of the rigid amorphous fraction and crystallinity on polylactide transport properties, Macromolecules 51 (2018) 3923–3931, https://doi.org/10.1021/acs.macromol.8b00833.

[47] H.C. Koh, J.S. Park, M.A. Jeong, H.Y. Hwang, Y.T. Hong, S.Y. Ha, S.Y. Nam, Preparation and gas permeation properties of biodegradable polymer/layered silicate nanocomposite membranes, Desalination 233 (2008) 201–209, https://doi.org/10.1016/j.desal.2007.09.043.

[48] M.A. Ortenzi, L. Basilissi, H. Farina, G. Di Silvestro, L. Piergiovanni, E. Mascheroni, Evaluation of crystallinity and gas barrier properties of films obtained from PLA nanocomposites synthesized via "in situ" polymerization of l-lactide with silane-modified nanosilica and montmorillonite, Eur. Polym. J. 66 (2015) 478–491, https://doi.org/10.1016/j.eurpolymj.2015.03.006.

[49] J.-W. Rhim, S.-I. Hong, C.-S. Ha, Tensile, water vapor barrier and antimicrobial properties of PLA/nanoclay composite films, LWT - Food Sci. Technol. (Lebensmittel-Wissenschaft -Technol.) 42 (2009) 612–617, https://doi.org/10.1016/j.lwt.2008.02.015.

[50] R.L. Hamilton, Water vapor permeability of polyethylene and other plastic materials, Bell System Technical Journal 46 (1967) 391–415, https://doi.org/10.1002/j.1538-7305.1967.tb01064.x.

[51] M.L. De Haro, J.A.P. Del Río, S. Whitaker, Flow of Maxwell fluids in porous media, Transport Porous Media 25 (1996) 167–192, https://doi.org/10.1007/BF00135854.

[52] S.A. Hashemifard, A.F. Ismail, T. Matsuura, Prediction of gas permeability in mixed matrix membranes using theoretical models, J. Membr. Sci. 347 (2010) 53–61, https://doi.org/10.1016/j.memsci.2009.10.005.

[53] T. Htira, S. Zid, M. Zinet, E. Espuche, Finite element analysis of gas diffusion in polymer nanocomposite systems containing rod-like nanofillers, Polymers 13 (2021) 2615, https://doi.org/10.3390/polym13162615.

[54] L.E. Nielsen, Models for the Permeability of Filled Polymer Systems, Journal of Macromolecular Science—Chemistry, 1967, https://doi.org/10.1080/10601326708053745.

[55] G. Choudalakis, A.D. Gotsis, Permeability of polymer/clay nanocomposites: a review, Eur. Polym. J. 45 (2009) 967–984, https://doi.org/10.1016/j.eurpolymj.2009.01.027.

[56] C. Thellen, C. Orroth, D. Froio, D. Ziegler, J. Lucciarini, R. Farrell, N.A. D'Souza, J. A. Ratto, Influence of montmorillonite layered silicate on plasticized poly(l-lactide) blown films, Polymer 46 (2005) 11716–11727, https://doi.org/10.1016/j.polymer.2005.09.057.

[57] F. Li, C. Zhang, Y. Weng, X. Diao, Y. Zhou, X. Song, Enhancement of gas barrier properties of graphene oxide/poly (lactic acid) films using a solvent-free method, Materials 13 (2020) 3024, https://doi.org/10.3390/ma13133024.

[58] A.M. Pinto, J. Cabral, D.A.P. Tanaka, A.M. Mendes, F.D. Magalhães, Effect of incorporation of graphene oxide and graphene nanoplatelets on mechanical and

gas permeability properties of poly(lactic acid) films, Polym. Int. 62 (2013) 33–40, https://doi.org/10.1002/pi.4290.
[59] J.C. Maxwell, A Treatise on Electricity and Magnetism, Clarendon Press, 1873.
[60] C. Courgneau, S. Domenek, R. Lebossé, A. Guinault, L. Avérous, V. Ducruet, Effect of crystallization on barrier properties of formulated polylactide, Polym. Int. 61 (2012) 180–189, https://doi.org/10.1002/pi.3167.
[61] H. Tsuji, Y. Tezuka, Stereocomplex Formation between enantiomeric poly(lactic acid)s. 12. Spherulite growth of low-molecular-weight poly(lactic acid)s from the melt, Biomacromolecules 5 (2004) 1181–1186, https://doi.org/10.1021/bm049835i.
[62] F. Nilsson, U.W. Gedde, M.S. Hedenqvist, Penetrant diffusion in polyethylene spherulites assessed by a novel off-lattice Monte-Carlo technique, Eur. Polym. J. 45 (2009) 3409–3417, https://doi.org/10.1016/j.eurpolymj.2009.09.018.